



UNIVERSITY OF LEEDS

This is a repository copy of *Development of an in-situ shaker for evaluating railway earthworks*.

White Rose Research Online URL for this paper:

<https://eprints.whiterose.ac.uk/218607/>

Version: Accepted Version

Article:

Lyu, P., Luo, Q., Feng, G. et al. (3 more authors) (2024) Development of an in-situ shaker for evaluating railway earthworks. *Soil Dynamics and Earthquake Engineering*, 179. 108550. ISSN 0267-7261

<https://doi.org/10.1016/j.soildyn.2024.108550>

© 2024, Elsevier. This manuscript version is made available under the CC-BY-NC-ND 4.0 license <http://creativecommons.org/licenses/by-nc-nd/4.0/>. This is an author produced version of an article published in *Soil Dynamics and Earthquake Engineering*. Uploaded in accordance with the publisher's self-archiving policy.

Reuse

This article is distributed under the terms of the Creative Commons Attribution-NonCommercial-NoDerivs (CC BY-NC-ND) licence. This licence only allows you to download this work and share it with others as long as you credit the authors, but you can't change the article in any way or use it commercially. More information and the full terms of the licence here: <https://creativecommons.org/licenses/>

Takedown

If you consider content in White Rose Research Online to be in breach of UK law, please notify us by emailing eprints@whiterose.ac.uk including the URL of the record and the reason for the withdrawal request.



eprints@whiterose.ac.uk
<https://eprints.whiterose.ac.uk/>

Development of an In-situ Shaker for Evaluating Railway Earthworks

Pengju Lyu

1. School of Civil Engineering, Southwest Jiaotong University, Chengdu 610031, China
E-mail: LvPengju@my.swjtu.edu.cn

Qiang Luo

1. School of Civil Engineering, Southwest Jiaotong University, Chengdu 610031, China;
2. Key Laboratory of High-speed Railway Engineering (Southwest Jiaotong University), Ministry of Education, Chengdu 610031, China
E-mail: LQrock@swjtu.edu.cn

Guishuai Feng

1. School of Civil Engineering, Southwest Jiaotong University, Chengdu 610031, China
E-mail: fgs@my.swjtu.edu.cn

David P. Connolly

3. School of Civil Engineering, University of Leeds, Leeds LS2 9JT, UK
Email: D.Connolly@leeds.ac.uk

Kaiwen Liu*

1. School of Civil Engineering, Southwest Jiaotong University, Chengdu 610031, China;
2. Key Laboratory of High-speed Railway Engineering (Southwest Jiaotong University), Ministry of Education, Chengdu 610031, China
E-mail: kaiwen.liu@queensu.ca (*Corresponding author)

Tengfei Wang

1. School of Civil Engineering, Southwest Jiaotong University, Chengdu 610031, China;
2. Key Laboratory of High-speed Railway Engineering (Southwest Jiaotong University), Ministry of Education, Chengdu 610031, China
E-mail: w@swjtu.edu.cn; ORCID: 0000-0003-4079-0687

1 **Abstract**

2 The geotechnical and geodynamic characteristics of railway earthworks under train loading are
3 important quantities for railway and geotechnical engineers, but difficult to quantify. Characterizing
4 the anticipated settlement and dynamic properties of compacted fills after earthwork construction, but
5 before track laying, is advantageous, because modifying construction after laying the track is
6 significantly more expensive. The difficulty in measuring these indices arises from the need to perform
7 cyclic loading that realistically simulates the frequencies and magnitudes induced by trains. To address
8 this issue, this paper introduces a novel shaker designed to apply cyclic loads similar to those of trains.
9 The paper first presents an outline of the design requirements for the shaker, followed by the
10 development of a theoretical dynamics model to aid mechanical design. This model is used for
11 examining various shaker configurations, especially their performance under different potential testing
12 conditions. The shaker's final design includes dual eccentric rotors that excite an adjustable-mass
13 counterweight, complemented by a lateral support frame to counter horizontal movement and ensure
14 vertical excitation. Once the shaker is built, it is used to evaluate newly constructed mudstone
15 earthworks near a railway line. A method for estimating the dynamic stiffness and damping of
16 earthworks is proposed, which uses data from frequency sweep test data from the shaker. Outputs from
17 the dynamics model show close alignment with the field results. Finally, a method for designing the
18 shaker configuration according to the desired loads is proposed.

19 **Keywords:** Railway Earthworks; Non-Destructive Testing; Dual-Rotor Shaker; Frequency Sweep; Fill
20 Compaction

Nomenclature

C_Z, C_ψ	Damping coefficients in Z and ψ directions for the vibrating system	n_0	Synchronous speed of motor (rpm)
c_f	Damping coefficients of foundation per unit area	n_N	Rated speed of motor (rpm)
f	Frequency of electrical power supply	P_N	Motor's rated power
f'	Rotational frequency of eccentric rotors	p	Number of pole pairs in the motor
f_N	Rated frequency of motor	p_s	Induced stress under the loading plate on the foundation
f_i	Axis damping coefficients for motors, where $i = 1, 2$	p_v	Minimum value of p_s
g	Gravitational acceleration	p_{p-v}	Peak-to-valley value of p_s
J_a	Total moment of inertia of vibrating system about its center of mass	r	Eccentric rotor's radius
J_i	Combined moment of inertia of eccentric rotor and motor shaft	r_b	Radius of bottom of loading plate
$J_{self,k}$	Individual moments of inertia for shaker components about their respective centers of mass	s	Motor slip
$J_{O,k}$	Moments of inertia for shaker components relative to the shaker's center of mass	s_N	Motor's rated slip
J_M	Moment of inertia for shaker, excluding the eccentric rotors	s_M	Motor's critical slip
J_{O_i}	Motor shaft's moments of inertia	s_M'	Critical slip after reducing motor's supply frequency
K_Z, K_ψ	Stiffness coefficients in Z and ψ directions for the vibrating system	T_{ei}	Electromagnetic torque generated by the motor, where $i = 1, 2$
k_f	Foundation stiffness coefficients per unit area	T_M	Motor's maximum torque output
l	Distance from rotor's rotational center to shaker's center of mass	T_N	Motor's rated torque output
l_e	Distance between motor shafts	Z	Shaker's vertical displacement
m_i	Mass of each eccentric rotor, where $i = 1, 2$	α	Phase difference between the two eccentric rotors
m	Mass of eccentric rotor when $m_1 = m_2$	α_m	Maximum absolute value of phase difference
m_e	Mass of an individual eccentric block	α_{MT}	Motor's overload coefficient
m_s	Mass of an individual counterweight block	β	Angle between line O_iO' and shaker's horizontal axis ($x'O'y'$)
M	Total mass of shaker, including motors, framework, loading plate, and counterweights	β_a	Amplification multiplier
M_a	Combined mass of the vibrating system, inclusive of m_1 and m_2	φ_i	Phase angle of eccentric rotor, where $i = 1, 2$
n_e	Number of eccentric blocks on one end of a motor	ψ	Shaker's swing angle
n_s	Total number of counterweight blocks	ω	Eccentric rotor's angular frequency
n	Rotational speed of both the motor and the eccentric rotor (rpm)		

23 **1. Introduction**

24 Long-term, repeated train loading influences the stability and durability of railway substructures [1].
25 The cost of repairing earthworks after track installation can be considerable. Therefore, understanding
26 the mechanical performance of these earthworks is crucial for optimizing the construction, operation,
27 and maintenance economies of railway. Although wayside monitoring during train passage [2–4]
28 provides useful insights, it can be costly and challenging to implement [5,6]. Mathematical models
29 [1,7,8] and finite element methods [9–11] serve as cost-effective and convenient alternatives. However,
30 these methods often involve simplifications and are dependent upon reliable input properties which
31 are often difficult to measure [5,12,13].

32 An alternative approach is to use laboratory test platforms to simulate train loading on large-scale
33 trackbed samples [14–16]. However, the challenge with this is the complex testing equipment required
34 and boundary effects caused by the limited testing sample dimensions. Further, in a laboratory
35 environment it can be difficult to construct track-earthwork test samples in the same manner as
36 performed on-site. For example, large compaction plant can be challenging to operate in a laboratory
37 space.

38 Considering the challenges with laboratory tests and numerical analysis, Miwa and Yoshimura [17]
39 developed a vehicle-borne mechanical system which incorporated hydraulic actuators between the
40 train and rail to serve as mechanical vibration shakers, simulating the vehicle's impact on the track
41 structure. However, most alternative field shakers have employed inertial mechanisms to excite the
42 track or earthworks, generating excitation through rotating eccentric rotors powered by electric motors.
43 Wang [12] and Wang et al. [13], for instance, used an inertial shaker equipped with a drive system,

44 circulating cooling system, and electric control system, to assess the dynamic performance of a novel
45 structure tailored for expansive soil subgrade. Huang et al. [18] employed the same shaker to
46 investigate the vibration characteristics of a ballasted railway subgrade supported by a pile-slab
47 composite foundation [19,20]. Zhang et al. [21] applied an inertial excitation device to simulate the
48 axial loads from a single bogie on an embankment filled with weathered red mudstone. Through
49 excitation tests, the study evaluated the dynamic stresses, displacements, and accelerations of the
50 railway track-subgrade system. In addition, Cai et al. [22] applied an inertial shaker which used a large
51 volume of rectangular concrete as both base and counterweight to investigate the suitability of cement-
52 improved expansive soil for use as fill material for heavy-haul railway subgrade. Ye et al. [23]
53 employed a similar shaker to study the stress and deformation characteristics of a track-asphalt-
54 concrete-subgrade system under varying temperature and train loading. While these shakers have
55 found application in railway foundation research, most studies focus on stress and permanent
56 deformation. Comprehensive analyses that include the dynamics of the entire system, comprising both
57 the shaker and the foundation, as well as verification of the shaker's output force, remain scarce.

58 Regarding mechanical shakers, extensive research has been performed on the different types of
59 vibrating equipment, including vibrating screen systems [24], vibrating mills [25], and vibrating
60 conveyors [26], among others [27–30]. These systems commonly employ a dynamic model simplified
61 as a rigid mass block. This block is constrained by springs and dampers and is excited by the rotation
62 of at least two eccentric rotors. The system's overall response is determined through a combination of
63 theoretical, simulation, and experimental methods. Importantly, the shafts driving these eccentric
64 rotors need not be mechanically interlinked through meshing gears. Under specific conditions, the

65 rotor rotations can sustain a stable phase difference, thereby generating the necessary excitation for
66 industrial applications. Consequently, the configuration may allow for the omission of a cooling system
67 installed for the eccentric rotor connecting element employed by shakers in railway dynamic tests
68 [12,21], offering a potential for cost savings. This research methodology coupled with the
69 implementation of eccentric rotor arrangements without engagement, holds promise for the
70 development of excitation equipment for railway applications.

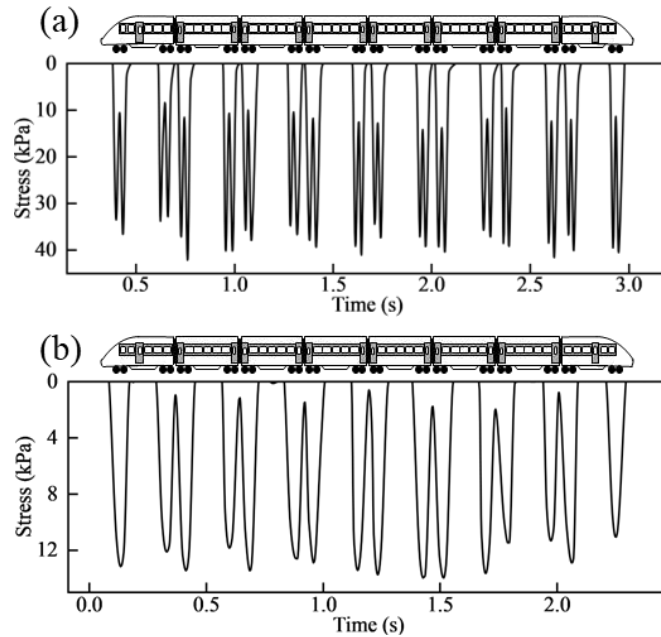
71 Thus, this study introduces a design for a dual-rotor shaker optimized for the dynamic testing of
72 railway earthworks. It is novel because it eliminates the need for meshing gears and other
73 interconnections between eccentric rotors. The foundation is conceptualized as a damped spring, and
74 Lagrange's equation is used to formulate differential equations that describe the dynamic behavior of
75 the vibrating system. A simulation study is used to provide insights into the shaker's operational state
76 and investigates the phase differences between the two eccentric rotors under differing potential testing
77 conditions. A physical prototype, constructed according to the design, is used for in-situ tests on
78 strongly weathered red-bed mudstone. A comparative analysis focuses on both the output stress
79 generated by the shaker and the synchronization of its eccentric rotors, drawing upon test and
80 simulation data. Additionally, this study proposes method for estimating soil stiffness and damping
81 utilizing field test data, alongside technique for designing shaker configurations based on specific load
82 requirements.

83 **2. Design considerations**

84 This section presents stress distribution characteristics in railway track foundations and addresses
85 dynamic testing shaker design requirements. It concludes by presenting a concept shaker design.

86 **2.1. Characteristics of train loading**

87 Train loading is transferred to the foundation surface via the track structure. A typical stress-time curve
88 of the track foundation surface is depicted in Fig. 1 [3,16,31]. The data is from the traversal of a train
89 comprising two locomotives, positioned at each extremity, and six intermediate coaches, resulting in
90 a total of 16 bogies and 32 axles [3,31]. Fig. 1a illustrates that for ballasted tracks, the number of peak
91 stresses corresponds to the train's axle count. Fig. 1b demonstrates that for slab tracks, the number of
92 peak stresses is equal to the bogie count. For ballasted and slab track foundation, the stress experienced
93 during a single loading and unloading cycle is predominately implemented by an individual axle and
94 bogie, respectively. This is caused by the increased bending stiffness of the concrete slab compared to
95 the ballast. Depending upon the configuration of train, after several loading and unloading cycles, there
96 may be a pause before the next one begins in the stress. Hence, the distribution of stress-time curves
97 on track foundation surface due to train loading is influenced by several parameters. These include the
98 car length, the distance between bogies, the axle spacing within bogies, the train speed, as well as track
99 irregularities and the axle weight [8,32,33]. Furthermore, the dynamic loading of an actual train covers
100 a broad frequency range [16,32].

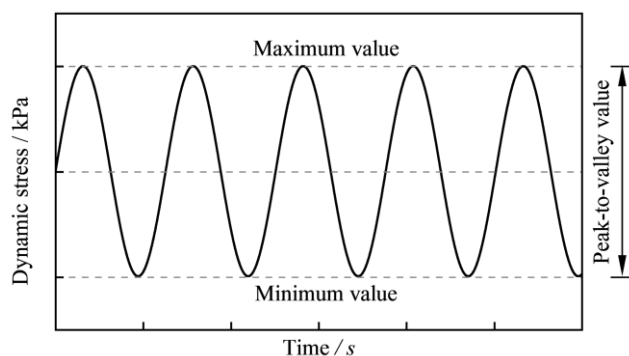


101
 102 **Fig. 1.** Measured stress-time curve of the subgrade surface due to train loading for (a) ballasted track [3] and (b)
 103 slab track [16,31].

104 **2.2. Design requirements for shaker loading**

105 The stress produced in the track foundation by the train can be primarily boiled down to frequencies
 106 and amplitudes of stress [16,32]. The selection of specific frequency and amplitude depends on the
 107 potential operating scenarios of the railway earthworks under evaluation. In evaluating earthworks for
 108 both ballasted and slab track foundations, current shaker methods typically simulate train loading using
 109 harmonic excitation characterized by a single amplitude and frequency [12,13,18,21–23]. Fig. 2
 110 illustrates a dynamic stress-time curve of a sinusoidal wave. Within the context of train loading
 111 simulation, the minimum stress reflects stress from the superstructure's self-weight, and maximum
 112 stress represents the total stress when train loading is considered. The difference between these, namely
 113 the peak-to-valley value, approximately simulates train loading. In addition to magnitude, load
 114 frequency also influences a structure's response. Specifically, when the load frequency aligns with the
 115 structure's natural frequency, this synchrony greatly amplifies the load's impact, potentially leading to

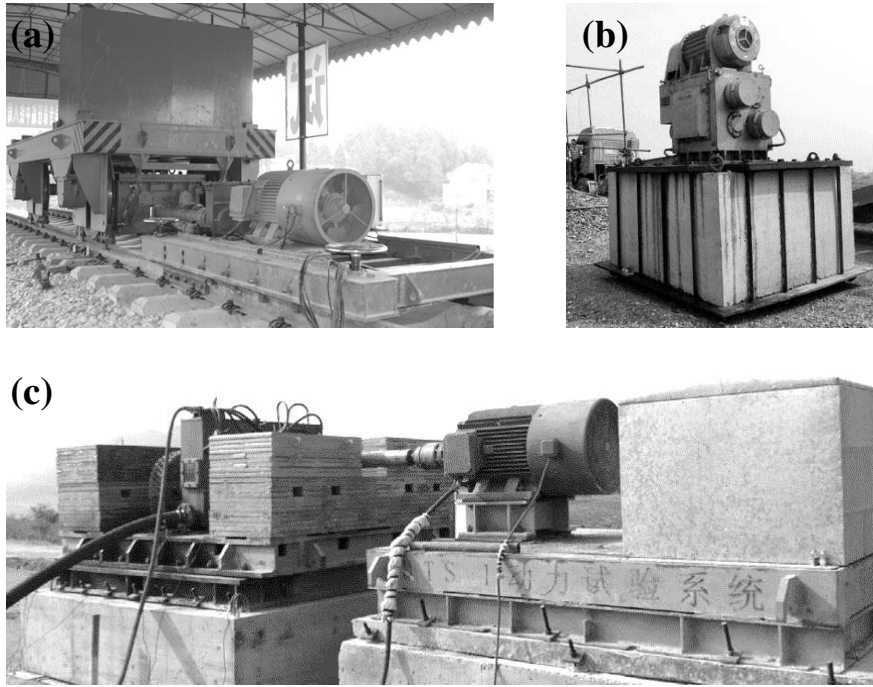
116 a resonance phenomenon. This can severely compromise structural safety. Thus, it is crucial to account
117 for load frequency while simulating the effects of train loading. The simple harmonic wave frequency
118 is related to the speed of the train being simulated.



119

120 **Fig. 2.** Sinusoidal dynamic stress time curve.

121 Inertia-type shakers are commonly used to generate this type of harmonic loading. Using a shaker to
122 produce consistent repeated loading for simulating train-induced stresses allows for accelerated testing
123 and studying earthworks settlement. Additionally, employing the shaker to sweep across a spectrum of
124 frequencies aids in assessing the dynamic properties of soil, involving stiffness and damping, which
125 are crucial for setting parameters in numerical simulations [1,7,8]. Fig. 3 shows three inertial shakers
126 used in railway earthwork research to produce cyclic loading.



127

128 **Fig. 3.** Inertia-type shakers in railway earthwork dynamic testing: (a) ZSS50 [34];(b) SBZ60 [22]; (c) DTS-1 [12].

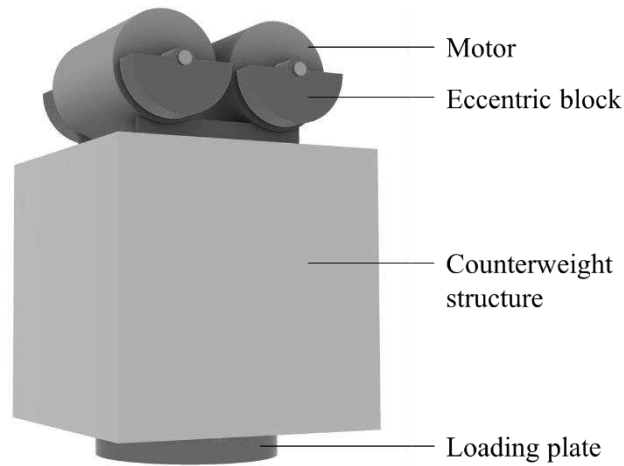
129 The *Code for Design of Railway Earth Structure* (TB10001-2016) stipulates that stresses on the track
 130 foundation surface due to the self-weight of the track range from 11.6 kPa to 14.3 kPa for slab tracks
 131 and 17.3 kPa to 23.3 kPa for ballasted tracks. In addition, the peak values of stresses on a slab track
 132 subgrade surface due to train loading generally range from 13 kPa to 20 kPa, while those for ballasted
 133 tracks vary between 50 kPa and 100 kPa [35]. The minimum value of the stress output from the shaker
 134 should at least match the self-weight of the track structure, with a minimum threshold of 11.6 kPa.
 135 Additionally, the peak-to-valley value of stress output from the shaker should surpass the train-induced
 136 stress, setting its minimum at no less than 13 kPa.

137 Studies available related to track foundation dynamics lack a definitive correlation between single-
 138 frequency loading and the frequency of train-induced loading. Zhang et al. [21] in their field
 139 experiments with the ZSS50 shaker (Fig. 3a) used a frequency of 15 Hz. Alternatively, Cai et al. [22]
 140 calculated the vibration frequency for dynamic tests with SBZ60 shaker (Fig. 3b) from the ratio of

141 vehicle speed to axle spacing. Further, Wang [12] conducted a frequency sweep dynamic test on the
142 subgrade, varying between 5~23 Hz with the DTS-1 shaker (Fig. 3c). Zhang [36] recommended using
143 single-frequency loading at frequency that result in cumulative settlements identical to those caused
144 by train loading. It may be viable to consider the dominant frequencies for the track foundation under
145 a moving train as equivalent frequencies. Regarding slab track, the dominant frequencies are
146 approximately 1.2 Hz and 3.6 Hz at a train speed of 108 km/h, around 2.4 Hz and 7.2 Hz for 216 km/h,
147 and close to 4 Hz and 12 Hz for 360 km/h [16]. Based on the above studies, it is advised to design
148 shakers capable of delivering loads at a maximum frequency of at least 25 Hz.

149 **2.3. Initial design**

150 Considering the typical characteristics of train and track loading, a novel conceptual model of a dual-
151 rotor shaker for the dynamic testing of railway earthworks is shown in Fig. 4. It consists of two
152 independent asynchronous electric motors mounted symmetrically on top of a counterweight structure,
153 which drive eccentric blocks with equal mass, generating cyclic excitations. In contrast to the shakers
154 depicted in Fig. 3, the uniqueness is the absence of mechanical coupling between the two motors, thus
155 offering efficiencies in operation and maintenance. When the eccentric blocks, driven by the two
156 motors, rotate in opposing directions at equal speeds, and the center of mass remains consistently
157 symmetrical with respect to the plane between the two motors, synchronous rotation of the eccentric
158 blocks is achieved. As a result of the eccentric block's synchronous rotation, a harmonic variation in
159 the vertical direction of the resultant force is observed, while the horizontal direction maintains a null
160 force, thus introducing harmonic excitation into the soil.



161
 162 **Fig. 4.** Conceptual diagram of shaker.

163 The excitation of eccentric blocks is directly linked to their mass, eccentric radius, and rotation speed.
 164 Manufacturing eccentric blocks with a uniform shape is a practical approach and allows for the
 165 modulation of excitation intensity by changing the number of blocks engaged. The excitation intensity
 166 can also be changed by altering the supply frequency. The counterweight structure for the motors
 167 should have sufficient mass to counterbalance the upward force generated by the eccentric blocks,
 168 ensuring the shaker always remains in contact with the ground. Additionally, the mass of this structure
 169 must be variable to adjust the maximum and minimum values of the output force from the shaker. In
 170 addition, to effectively transfer the output force from the shaker to the soil, a loading plate may be
 171 situated beneath the counterweight structure. Ideally the design and configuration of the loading plate
 172 should be adaptable, allowing for alteration to match the required load distribution pattern.
 173 Incorporating variable-mass eccentric blocks and a counterweight structure, as well as a replaceable
 174 loading plate improves the equipment's adaptability.

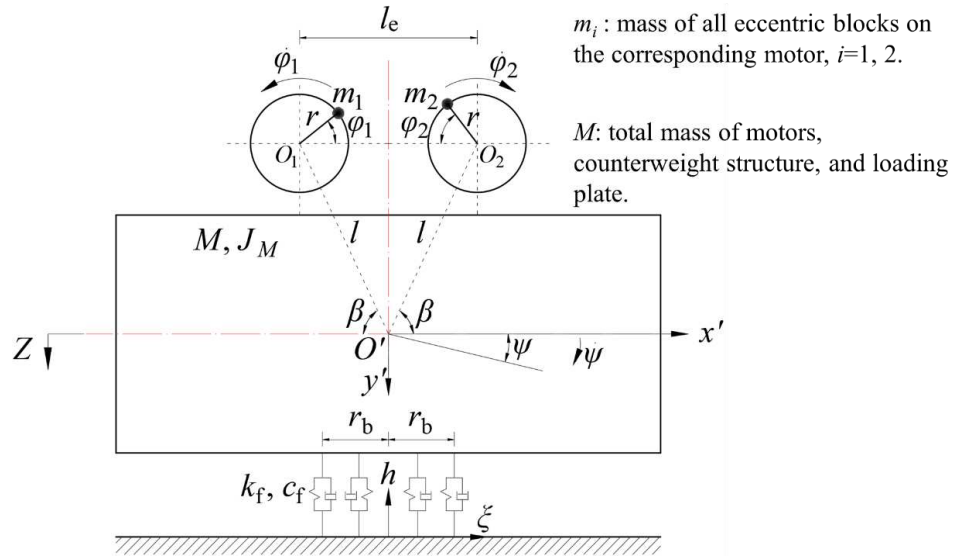
175 **3. Conceptual model**

176 This section develops a conceptual mathematical model of the earthworks shaker, for the purposes of

177 informing the mechanical system design. The methodology for determining parameters within this
178 model is outlined. Subsequently, it explicates the application of explicit integration technique [37] in
179 solving the relevant differential equations of the model. The explicit integration technique possesses
180 both accuracy and efficiency in the resolution of nonlinear differential equations [1,7,38].

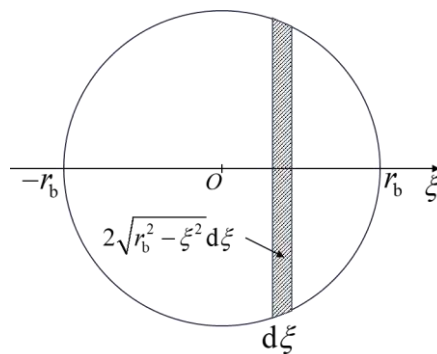
181 **3.1. Dual-rotor shaker dynamics and foundation interaction**

182 The general concept of the shaker is to use motor-driven eccentric blocks to excite a large
183 counterweight to excite earthworks at a given frequency. Only vertical excitation is required meaning
184 lateral displacement of the shaker must be minimised. Hence, Fig. 5 shows the dynamic model created
185 for the shaker, focusing on the vertical displacement (Z) and swing angle (ψ) of the shaker and omitting
186 horizontal displacement. The model incorporates two eccentric rotors, each with a specified eccentric
187 radius r and mass m_i , rotating in opposite directions, where $i = 1,2$. All potential additional components
188 (e.g. motors, counterweight structure, and loading plate) are considered as a unified rigid mass block
189 with mass M . The instantaneous phase angle ϕ_i indicates the eccentric rotor's rotation relative to its
190 center O_i . l represents the distance from point O_i to the mass center O' of shaker, and l_e is the separation
191 between points O_i . The angle between line O_iO' and the horizontal axis of $x'O'y'$ affixed to the apparatus
192 is signified by β . Finally, the foundation is modelled as a parallel spring system under the loading plate,
193 influenced by viscous damping, with stiffness coefficients K_Z and K_ψ for the Z - and ψ - directions,
194 respectively, along with damping coefficients C_Z and C_ψ .



195
196 **Fig. 5.** Dynamic model of dual-rotor shaker.

197 The coordinate axis ξ perpendicular to the motor shaft originates at the center of the lower surface of
 198 loading plate, as illustrated in Fig. 5. The coordinates for points on the loading plate sharing the same
 199 elevation with the non-displaced horizontal foundation surface are calculated as $\xi_c = -Z / \psi$, based
 200 on instantaneous values of Z and ψ . ξ_c enables real-time updates to K_Z , K_ψ , C_Z and C_ψ . Subsequently,
 201 non-linear interaction between the foundation surface and the shaker base can be considered. As an
 202 example, the circular loading plate with radius r_b shown in Fig. 6 will be used to illustrate how to
 203 update K_Z , K_ψ , C_Z and C_ψ based on the ξ_c values.



204
205 **Fig. 6.** Coordinate axis representation on circular loading plate bottom.

206 The parallel spring assembly representing the foundation under the shaker's base exhibits stiffness k_f

207 and damping c_f per unit area. The shaded region depicted in Fig. 6 represents the loading plate's area
 208 within the interval $[\xi, \xi+d\xi]$, measuring $2\sqrt{r_b^2 - \xi^2} d\xi$. The equivalent stiffness and damping of the
 209 foundation with shaded area in contact with the loading plate are $2k_f \sqrt{r_b^2 - \xi^2} d\xi$ and $2c_f \sqrt{r_b^2 - \xi^2} d\xi$,
 210 respectively. In the scenario where $\psi \geq 0$ (or $\psi < 0$), the shaker maintains contact with the substrate,
 211 corresponding to $\xi_c < -r_b$ (or $\xi_c > r_b$). Here, K_Z, K_ψ, C_Z and C_ψ are determined according to Eq. (1). In
 212 instances where partial separation occurs between the shaker base and the foundation surface,
 213 corresponding to $-r_b \leq \xi_c \leq r_b$, Eq. (1) is modified by adjusting the lower (or upper) integration limits
 214 to ξ_c for ascertaining K_Z, K_ψ, C_Z and C_ψ accurately. In cases of complete separation, denoted by ξ_c
 215 $> r_b$ (or $\xi_c < -r_b$), all these parameters reset to zero.

$$216 \quad \begin{cases} K_Z = 2k_f \int_{-r_b}^{r_b} \sqrt{r_b^2 - \xi^2} d\xi \\ K_\psi = 2k_f \int_{-r_b}^{r_b} \xi^2 \sqrt{r_b^2 - \xi^2} d\xi \\ C_Z = 2c_f \int_{-r_b}^{r_b} \sqrt{r_b^2 - \xi^2} d\xi \\ C_\psi = 2c_f \int_{-r_b}^{r_b} \xi^2 \sqrt{r_b^2 - \xi^2} d\xi \end{cases} \quad (1)$$

217 3.2. Equations of motion

218 The coordinates of the two eccentric rotors within the $x'O'y'$ coordinate system can be expressed using
 219 Eq. (2).

$$220 \quad \begin{cases} \Phi_1' = \begin{bmatrix} -l \cos \beta + r \cos \varphi_1 \\ -l \sin \beta - r \sin \varphi_1 \end{bmatrix} \\ \Phi_2' = \begin{bmatrix} l \cos \beta - r \cos \varphi_2 \\ -l \sin \beta - r \sin \varphi_2 \end{bmatrix} \end{cases} \quad (2)$$

221 In the $x'O'y'$ coordinate system, which is integral to the oscillating mechanism, real-time motion occurs
 222 along the Z - and ψ -directions. The transformation relations outlined in Eq. (3) clarify the spatial

223 coordinates of the eccentric rotors within the fixed coordinate system, culminating in the formulation
 224 presented in Eq. (4).

$$225 \quad \Phi_i = \begin{bmatrix} 0 \\ Z \end{bmatrix} + \begin{bmatrix} \cos \psi & -\sin \psi \\ \sin \psi & \cos \psi \end{bmatrix} \Phi_i' \quad (3)$$

$$226 \quad \left\{ \begin{array}{l} \Phi_1 = \begin{bmatrix} -l \cos(\beta + \psi) + r \cos(\varphi_1 - \psi) \\ Z - l \sin(\beta + \psi) - r \sin(\varphi_1 - \psi) \end{bmatrix} \\ \Phi_2 = \begin{bmatrix} l \cos(\beta - \psi) - r \cos(\varphi_2 + \psi) \\ Z - l \sin(\beta - \psi) - r \sin(\varphi_2 + \psi) \end{bmatrix} \end{array} \right. \quad (4)$$

227 Eq. (5) defines the kinetic energy T of the system:

$$228 \quad T = \frac{1}{2} M \dot{Z}^2 + \frac{1}{2} J_M \dot{\psi}^2 + \frac{1}{2} \sum_{i=1}^2 J_{O_i} \dot{\varphi}_i^2 + \frac{1}{2} \sum_{i=1}^2 m_i \dot{\Phi}_i^T \dot{\Phi}_i \quad (5)$$

229 where J_M signifies the moments of inertia of the rigid frame around its mass center, while J_{O_i} represents
 230 the shaft's inertia moments of motor i , $i=1, 2$.

231 In the system, the natural positions of the springs serve as zero potential energy reference points
 232 for both elastic and gravitational fields. Eq. (6) formulates the total potential energy U :

$$233 \quad U = \frac{1}{2} K_Z Z^2 + \frac{1}{2} K_\psi \psi^2 - M_a g Z \quad (6)$$

234 where $M_a = M + m_1 + m_2$ and acceleration of gravity g of 9.8 m/s^2 is assumed.

235 The viscous dissipation function D , originating from the energy exchange in the springs and
 236 motor shaft friction, is presented in Eq. (7):

$$237 \quad D = \frac{1}{2} C_Z \dot{Z}^2 + \frac{1}{2} C_\psi \dot{\psi}^2 + \frac{1}{2} f_1 \dot{\varphi}_1^2 + \frac{1}{2} f_2 \dot{\varphi}_2^2 \quad (7)$$

238 where f_1 and f_2 stand for the axis damping coefficients for the induction motors driving eccentric rotors
 239 1 and 2, respectively.

240 The system's generalized coordinates are shown in Eq. (8), while Eq. (9) defines the generalized
 241 force matrix. Here, T_{e1} and T_{e2} represent the electromagnetic torques driving eccentric rotors 1 and 2,

242 respectively.

$$243 \quad \mathbf{q} = [Z \ \psi \ \varphi_1 \ \varphi_2] \quad (8)$$

$$244 \quad \mathbf{P} = [0 \ 0 \ T_{e1} \ T_{e2}] \quad (9)$$

245 Finally, the generalized Lagrange's equation [27] as expressed in Eq. (10) is used to establish the
246 system's dynamic differential equations.

$$247 \quad \frac{d}{dt} \left(\frac{\partial(T-U)}{\partial \dot{\mathbf{q}}} \right) - \frac{\partial(T-U)}{\partial \mathbf{q}} + \frac{\partial D}{\partial \dot{\mathbf{q}}} = \mathbf{P} \quad (10)$$

248 In mechanical vibration studies, it is commonly observed that $\psi \ll 1$ [27,39]. This allows the
249 approximations $\sin \psi \approx 0$ and $\cos \psi \approx 1$ when expanding the dynamic equations obtained by
250 substituting Eqs. (4) through (9) into Eq. (10). Subsequently, in the dynamic model where $m_i \ll M$, the
251 equation of motion for the system is derived as shown in Eq. (11), following the further simplification
252 of the expanded dynamic equations based on references [27,39,40]:

$$253 \quad \begin{cases} M_a \ddot{Z} + C_Z \dot{Z} + K_Z Z + r \sum_{i=1}^2 m_i (\dot{\varphi}_i^2 \sin \varphi_i - \ddot{\varphi}_i \cos \varphi_i) = M_a g \\ J_a \ddot{\psi} + C_\psi \dot{\psi} + K_\psi \psi + r \sum_{i=1}^2 (-1)^i m_i [\dot{\varphi}_i^2 l \sin(\varphi_i + \beta) + \ddot{\varphi}_i (r - l \cos(\varphi_i + \beta))] = 0 \\ J_1 \ddot{\varphi}_1 + f_1 \dot{\varphi}_1 \\ + m_1 r [-\ddot{Z} \cos \varphi_1 - \dot{\psi}^2 l \sin(\varphi_1 + \beta) - \ddot{\psi} (r - l \cos(\varphi_1 + \beta))] = T_{e1} \\ J_2 \ddot{\varphi}_2 + f_2 \dot{\varphi}_2 \\ + m_2 r [-\ddot{Z} \cos \varphi_2 - \dot{\psi}^2 l \sin(\varphi_2 + \beta) + \ddot{\psi} (r - l \cos(\varphi_2 + \beta))] = T_{e2} \end{cases} \quad (11)$$

254 where, $J_a = J_M + \sum m_i (r^2 + l^2)$, and $J_i = J_{O_i} + m_i r^2$, $i=1,2$.

255 Upon substituting the slip s as shown in Eq. (12), into Eq. (13) for torque T_e , the mathematical
256 relation between T_e and the rotational speed n of the three-phase asynchronous can be defined as shown
257 in Eq. (14) [41]:

258
$$s = \frac{n_0 - n}{n_0} \quad (12)$$

259
$$T_e = \frac{2T_M}{\frac{s}{s_M} + \frac{s_M}{s}} \quad (13)$$

260
$$T_e = \frac{2T_M s_M n_0 (n_0 - n)}{s_M^2 n_0^2 + (n_0 - n)^2} \quad (14)$$

261 where n_0 denotes the synchronous speed of the motor. T_M signifies the maximum torque output of the
 262 vibratory motor, which is mathematically defined as $T_M = \alpha_{MT} T_N$. α_{MT} denotes the overload coefficient
 263 of the motor and $T_N = (60P_N)/(2n_N\pi)$ presents the rated torque, while P_N and n_N represent the rated
 264 power and rotational speed of the motor, respectively. Moreover, $s_M = s_N (\alpha_{MT} + \sqrt{\alpha_{MT}^2 - 1})$ characterizes
 265 the critical slip of the motor, while s_N represents the rated slip ratio of the vibratory motor.

266 Upon reducing the power supply frequency of a vibration motor with a rated frequency f_N of 50
 267 Hz for variable-speed control, the power supply frequency transitions to f ($f \leq f_N$), with the variable T_M
 268 remaining unaltered. Substituting f into Eq. (15) and taking into account the number of pole pairs p
 269 present in the stator, n_0 can be recalibrated. Similarly, the critical slip becomes inversely related to the
 270 altered supply frequency, necessitating an update to s_M' as dictated by Eq. (16) [41]. Insertion of
 271 $n_i = 30\dot{\phi}_i / \pi$ into Eq. (14) allows for the calculation of the instantaneous electromagnetic torque T_{ei} ,
 272 $i=1, 2$, within the framework of the dynamic differential equations established in Eq. (11).

273
$$n_0 = \frac{60f}{p} \quad (15)$$

274
$$s_M' = \frac{f_N}{f} s_M \quad (16)$$

275 **3.3. Simulation parameters**

276 To define the variables shown in Fig. 5, the mass of system must be known. Each single eccentric
 277 block has a mass m_e and the individual counterweight block have a mass m_s . The mass m_i of each
 278 eccentric rotor (where $i=1, 2$) is modulated by altering the number of eccentric blocks n_e at each end
 279 of the motor. The shaker mass M encompasses the motors, counterweight structure, and loading plate,
 280 which are modulated by adjusting the quantity n_s of counterweight blocks. The masses m_i is computed
 281 in accordance with Eq. (17). Similarly, the mass M_s of counterweights is calculated using Eq. (18).

$$282 \quad m_i = 2n_e m_e \quad (17)$$

$$283 \quad M_s = n_s m_s \quad (18)$$

284 Owing to the system's bilateral symmetry, O' aligns with the central axis of symmetry. The elevation
 285 \bar{h} of O' relative to the bottom of shaker complies with Eq. (19).

$$286 \quad \bar{h} = \frac{\sum M_k h_k}{\sum M_k} \quad (19)$$

287 Here, M_k denotes the mass of each component of the shaker while h_k is the height of the centre of mass
 288 for each part of the shaker relative to the bottom of shaker.

289 The separation between the two motor shafts is l_e , while the vertical elevation of the motor shaft
 290 from the bottom of shaker is denoted by h_1 . Using Eq. (20), the distance l shown in Fig. 5 can be
 291 obtained.

$$292 \quad l = \sqrt{(h_1 - \bar{h})^2 + (l_e / 2)^2} \quad (20)$$

293 Eq. (21) provides the means to ascertain the angle β shown in Fig. 5.

$$294 \quad \beta = \arctan \frac{h_1 - \bar{h}}{l_e / 2} \quad (21)$$

295 The moment of inertia for a rigid body serves as a metric for its rotational inertia, dependent upon both

296 mass magnitude and spatial distribution. To facilitate computation, the various components of the
 297 shaker can be simplified into geometric bodies with regular shape and uniform mass distribution. For
 298 example, the vibratory motors and a circular loading plate can be modeled as homogeneous cylinders,
 299 while some other components can be generalized as cuboids. Their moments of inertia about their
 300 respective centroids ($J_{\text{self},k}$) can be easily obtained.

301 Using Eq. (22), the moments of inertia $J_{O',k}$ for each component of the shaker, relative to the centre
 302 of mass O' of the shaker, are:

$$303 \quad J_{O',k} = J_{\text{self},k} + M_k d_k^2 \quad (22)$$

304 where d_k^2 specifies the square of distance between the centroid of each component and O' .

305 The moment of inertia J_M of the shaker is subsequently derived by summing the individual
 306 moments of inertia, each relative to O' , as stipulated by Eq. (23).

$$307 \quad J_M = \sum J_{O',k} \quad (23)$$

308 **3.4. Numerical solutions**

309 To streamline the solution process, the differential equations governing the shaker vibration are
 310 arranged in matrix form, as shown:

$$311 \quad [M]\{\ddot{X}\} + [C]\{\dot{V}\} + [K]\{X\} = [P] \quad (24)$$

312 where the constituent elements of the matrices and vectors are elaborated upon in Eqs. (25) through
 313 (31).

$$314 \quad \{X\} = \{Z \ \psi \ \varphi_1 \ \varphi_2\}^T \quad (25)$$

$$315 \quad \{V\} = \{\dot{Z} \ \dot{\psi}^2 \ \dot{\varphi}_1^2 \ \dot{\varphi}_2^2\}^T \quad (26)$$

$$316 \quad \{\ddot{X}\} = \{\ddot{Z} \ \ddot{\psi} \ \ddot{\varphi}_1 \ \ddot{\varphi}_2\}^T \quad (27)$$

$$317 \quad [M] = \begin{bmatrix} M_a & 0 & -m_1 r \cos \varphi_1 & -m_2 r \cos \varphi_2 \\ 0 & J_a & -m_1 r(r-l \cos(\varphi_1 + \beta)) & m_2 r(r-l \cos(\varphi_2 + \beta)) \\ -m_1 r \cos \varphi_1 & -m_1 r(r-l \cos(\varphi_1 + \beta)) & J_1 & 0 \\ -m_2 r \cos \varphi_2 & m_2 r(r-l \cos(\varphi_2 + \beta)) & 0 & J_2 \end{bmatrix} \quad (28)$$

$$318 \quad [C] = \begin{bmatrix} C_z & 0 & m_1 r \sin \varphi_1 & m_2 r \sin \varphi_2 \\ 0 & 0 & -m_1 r l \sin(\varphi_1 + \beta) & m_2 r l \sin(\varphi_2 + \beta) \\ 0 & -m_1 r l \sin(\varphi_1 + \beta) & 0 & 0 \\ 0 & -m_2 r l \sin(\varphi_2 + \beta) & 0 & 0 \end{bmatrix} \quad (29)$$

$$319 \quad [K] = \begin{bmatrix} K_z & 0 & 0 & 0 \\ 0 & K_\psi & 0 & 0 \\ 0 & 0 & 0 & 0 \\ 0 & 0 & 0 & 0 \end{bmatrix} \quad (30)$$

$$320 \quad [P] = [M_a g \quad -C_\psi \dot{\psi} \quad T_{e1} - f_1 \dot{\varphi}_1 \quad T_{e2} - f_2 \dot{\varphi}_2]^T \quad (31)$$

321 An explicit integration method [37] was employed to solve the differential equations of motion for the
322 vibrating system. The integration scheme of this approach is outlined in Eq. (32).

$$323 \quad \begin{cases} \{X\}_{st+1} = \{X\}_{st} + \{\dot{X}\}_{st} \Delta t + (1/2 + \psi_{\text{int}}) \{\ddot{X}\}_{st} \Delta t^2 - \psi_{\text{int}} \{\ddot{X}\}_{st-1} \Delta t^2 \\ \{\dot{X}\}_{st+1} = \{\dot{X}\}_{st} + (1 + \varphi_{\text{int}}) \{\ddot{X}\}_{st} \Delta t - \varphi_{\text{int}} \{\ddot{X}\}_{st-1} \Delta t \end{cases} \quad (32)$$

324 Here, Δt denotes the time step and was selected as 10^{-3} s for solving the shaker's dynamic equations.
325 φ_{int} and ψ_{int} , set at 0.5, regulate the algorithm's stability and precision. The subscript 'st' marks the
326 current integration step. The vector $\{\dot{X}\}$ results from the temporal first-order derivative of $\{X\}$,
327 defined as $\{\dot{X}\} = \{\dot{Z} \quad \dot{\psi} \quad \dot{\varphi}_1 \quad \dot{\varphi}_2\}^T$. Special attention was given to managing the transformation between
328 $\{\dot{X}\}$ and $\{V\}$ throughout the solution process.

329 Incorporation of initial conditions into Eq. (24) yields Eq. (33), which defines the system's initial
330 acceleration. For the initialization of the integration procedure, the terms φ_{int} and ψ_{int} are set to zero at
331 the first-time step. Eq. (32) then facilitates the computation of the subsequent system displacements
332 and velocities.

333
$$\{\ddot{X}\}_0 = [M]_0^{-1}([P]_0 - [K]_0\{X\}_0 - [C]_0\{V\}_0) \quad (33)$$

334 Further, integrating Eq. (32) into Eq. (24) produces Eq. (34), which defines the state of the system at
 335 $(st+1)\times\Delta t$.

336
$$[M]_{st+1}\{\ddot{X}\}_{st+1} + [C]_{st+1}\{V\}_{st+1} + [K]_{st+1}\{X\}_{st+1} = [P]_{st+1} \quad (34)$$

337 And then, this computation evolves into Eq. (35):

338
$$\{\ddot{X}\}_{st+1} = [M]_{st+1}^{-1}\{\tilde{P}\}_{st+1} \quad (35)$$

339 with

340
$$\{\tilde{P}\}_{st+1} = [P]_{st+1} - [K]_{st+1}\{X\}_{st+1} - [C]_{st+1}\{V\}_{st+1}$$

341 In summary, iterative application of Eq. (32) and Eq. (35) enable the calculation of the discrete values
 342 for displacement, velocity, and acceleration at each time step, culminating in the numerical solution of
 343 the system.

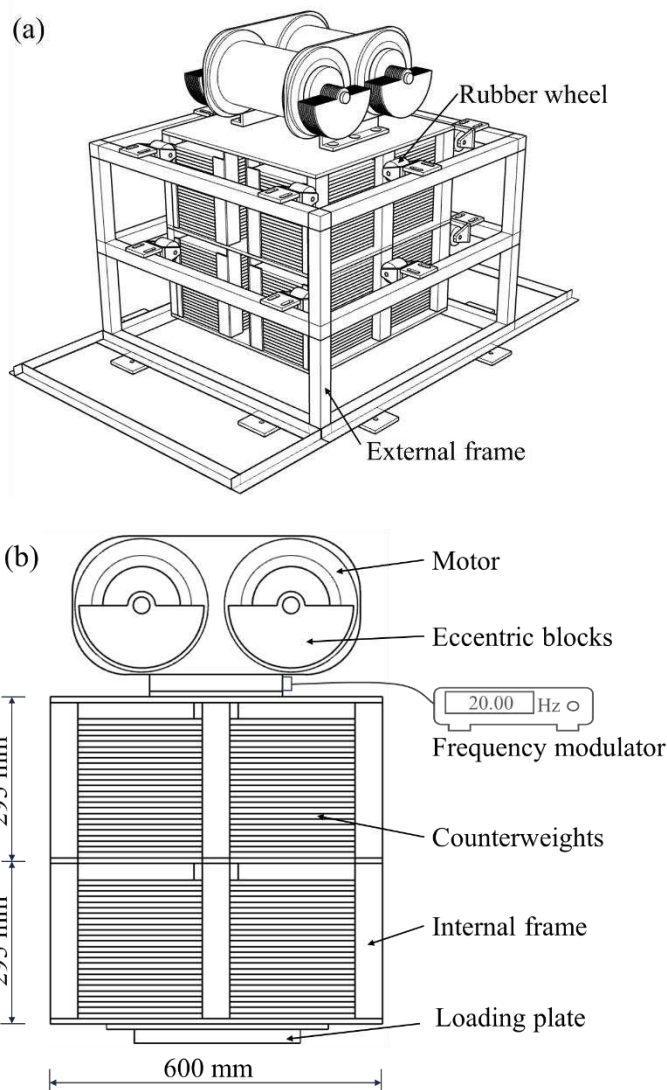
344 **4. Virtual development**

345 This section introduces the general mechanical design of the shaker. Next the dynamic behavior of it
 346 across three operational states is investigated. Then the influence of potential experimental variable
 347 uncertainties on the synchronous operation of the shaker's eccentric rotors is studied.

348 **4.1. Generalised mechanical design**

349 A generalised mechanical design for the shaker was developed as depicted in Fig. 7. As shown in Fig.
 350 7a, the device features two, three-phase asynchronous motors, each fitted with a maximum of 10
 351 eccentric blocks at one end. These motors are symmetrically mounted on an internal frame designed
 352 to accommodate counterweights. Adjacent to the internal frame's steel columns, an external frame
 353 equipped with rubber wheels ensures stability while permitting operational clearance. Fig. 7b provides

354 a detailed frontal view that identifies the various components of the apparatus. Motor speed control is
 355 managed through a frequency modulator connected to a 380 V, 50 Hz AC power supply. The internal
 356 frame dimensions are 600 mm × 600 mm × 590 mm and comprise three horizontal layers of rectangular
 357 steel plates, fortified by 11 vertical columns. This design creates eight zones for counterweight
 358 placement, each capable of accommodating up to 25 rectangular counterweights measuring 215 mm ×
 359 285 mm × 10 mm. A loading plate at the base of the internal frame is composed of two concentric,
 360 welded circular steel plates. The top plate measures 400 mm in diameter and 10 mm in thickness, while
 361 the bottom plate has a diameter of 300 mm and a thickness of 25 mm.

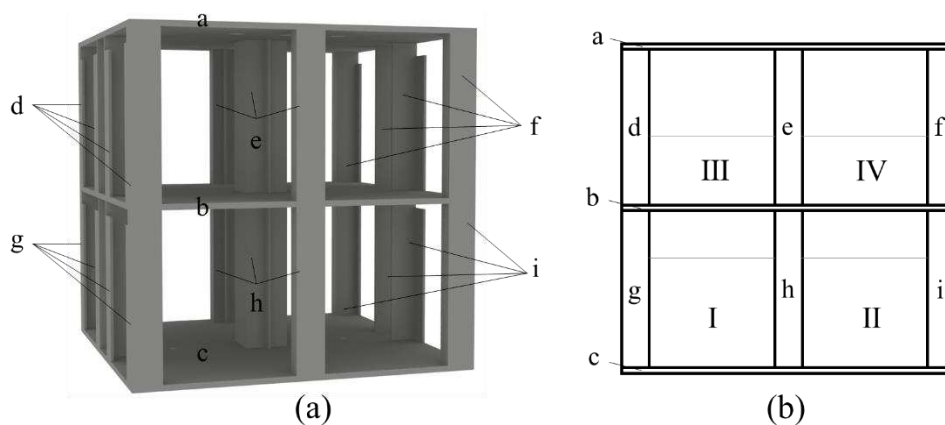


362

363

364 **Fig. 7.** Dual-rotor shaker design schematic: (a) perspective view; (b) front view.

365 Fig. 8 illustrates the inner framework for placing the counterweight blocks. As shown in Fig. 8a, the
 366 internal frame is segmented into 9 sections, identified as a to i. Sections a, b, and c correspond to three
 367 horizontal steel plates. The steel columns aligned identically in the frontal perspective are classified
 368 into six groups, from d to i. The mass of each column group is equally apportioned across the surface
 369 of the foremost plate. Likewise, the counterweights, identified from I to IV, have their masses evenly
 370 distributed across the areas of their front views. This approach simplifies the spatially non-uniform
 371 distribution of the internal frame and counterweight blocks into blocks with uniform mass distributions
 372 as depicted in Fig. 8b. This facilitates the calculation of the shaker's center of mass (O') and its moment
 373 of inertia (J_M). In practice, priority is placed on the equitable distribution of counterweights across the
 374 four pre-defined lower regions. Upon n_s being greater than the maximum quota of 100 for these lower
 375 zones, surplus counterweights are equally deployed in the upper regions.



376
 377 **Fig. 8.** Internal frame and counterweight division: (a) internal frame zoning; (b) schematic of the mass distribution.

378 Each eccentric block has a mass m_e of 889.11 g and an eccentricity radius r of 46 mm. The inner
 379 framework has a mass of 124.5 kg. Individual counterweight block has a mass m_s of 4.5 kg. The steel

380 plate in the upper section of the loading plate weighs 9.9 kg, while its lower counterpart has a mass of
381 13.8 kg. Excluding the eccentric blocks, the mass of each vibrating motor is 75 kg. The separation
382 between the two motor shafts (l_e) is 0.27 m. The component specifications for calculating the mass
383 center coordinates, moment of inertia of the shaker, and other parameters according to the methodology
384 in Section 3.3 are given in Table 1. In the formula for d_k^2 within Table 1, the first term represents the
385 square of the horizontal distance between the center of mass of the component in row and the shaker's
386 center of mass. The second term accounts for the square of the vertical distance between these two
387 centers of mass. In addition, the parameters for counterweights listed in Table 1 are calculated based
388 on whether the number of counterweight blocks (n_s) is greater than 100. For $n_s \leq 100$, the parameters
389 are defined as follows: $M_{12} = M_{13} = M_s/2$, $M_{14} = M_{15} = 0$, $h_{12} = h_{13} = 0.045 + 0.01n_s/8$, $J_{\text{self},12} = J_{\text{self},13} =$
390 $M_{12}(0.285^2 + (0.01n_s/4)^2)/12$, and $J_{\text{self},14} = J_{\text{self},15} = 0$. Conversely, for $n_s > 100$, the parameters are
391 adjusted as follows: $M_{12} = M_{13} = 100m_s/2$, $M_{14} = M_{15} = (n_s - 100)m_s/2$, $h_{12} = h_{13} = 0.045 + 0.01 \times 100/8$, h_{14}
392 $= h_{15} = 0.335 + 0.01(n_s - 100)/8$, $J_{\text{self},12} = J_{\text{self},13} = M_{12}(0.285^2 + (0.01 \times 100/4)^2)/12$, and $J_{\text{self},14} = J_{\text{self},15} =$
393 $M_{14}(0.285^2 + (0.01 \times (n_s - 100)/4)^2)/12$.

394 **Table 1.** Component specifications of the shaker

Components	No. k	M_k (kg)	h_k (m)	$J_{\text{self},k}$ (kg·m ²)	d_k^2 (m ²)	
Motor 1	1	75.0	0.790	0.304	$0.135^2 + (h_1 - \bar{h})^2$	
Motor 2	2	75.0	0.790	0.304	$0.135^2 + (h_2 - \bar{h})^2$	
Internal frame	a	28.3	0.620	0.8492	$0^2 + (h_3 - \bar{h})^2$	
	b	28.3	0.330	0.8492	$0^2 + (h_4 - \bar{h})^2$	
	c	28.3	0.040	0.8492	$0^2 + (h_5 - \bar{h})^2$	
	d	6	5.5	0.475	0.0371	$0.275^2 + (h_6 - \bar{h})^2$
	e	7	8.8	0.475	0.0593	$0^2 + (h_7 - \bar{h})^2$
	f	8	5.5	0.475	0.0371	$0.275^2 + (h_8 - \bar{h})^2$
	g	9	5.5	0.185	0.0371	$0.275^2 + (h_9 - \bar{h})^2$
	h	10	8.8	0.185	0.0593	$0^2 + (h_{10} - \bar{h})^2$
	i	11	5.5	0.185	0.0371	$0.275^2 + (h_{11} - \bar{h})^2$

Counterweights	I	12	M_{12}	h_{12}	$J_{\text{self},12}$	$0.149^2+(h_{12}-\bar{h})^2$
	II	13	M_{13}	h_{13}	$J_{\text{self},13}$	$0.149^2+(h_{13}-\bar{h})^2$
	II	14	M_{14}	h_{14}	$J_{\text{self},14}$	$0.149^2+(h_{14}-\bar{h})^2$
	IV	15	M_{15}	h_{15}	$J_{\text{self},15}$	$0.149^2+(h_{15}-\bar{h})^2$
Loading plate	Upper plate	16	9.9	0.030	0.0991	$0^2+(h_{16}-\bar{h})^2$
	Lower plate	17	13.8	0.0125	0.0783	$0^2+(h_{17}-\bar{h})^2$

395 The parameters for the vibratory motors are shown in Table 2. The motor's rotational speed n indicates
396 its revolutions per minute, whereby the rotation frequency, f' , is calculated as n divided by 60 seconds.
397 Initial simulations showed that n closely approximates the synchronous speed n_0 as defined by Eq.
398 (15). Thus, approximating n to be equivalent to n_0 , then f' is derived as the quotient of $60f/p$ and 60
399 seconds. Hence, the rotation frequency f' of the eccentric rotors powered by the shaker's motors,
400 characterized by two pole pairs, is approximated as $f/2$. The shaker generates excitation through the
401 combined action of two eccentric rotors rotating at a frequency denoted by f' . When these rotors
402 operate in synchronization, the excitation frequency of the shaker matches f' . The two vibration motors,
403 having a rated frequency (f_N) of 50 Hz, may generate excitations up to a maximum frequency of 25 Hz
404 and a peak force of 40 kN.

405 **Table 2.** Vibration motor parameters

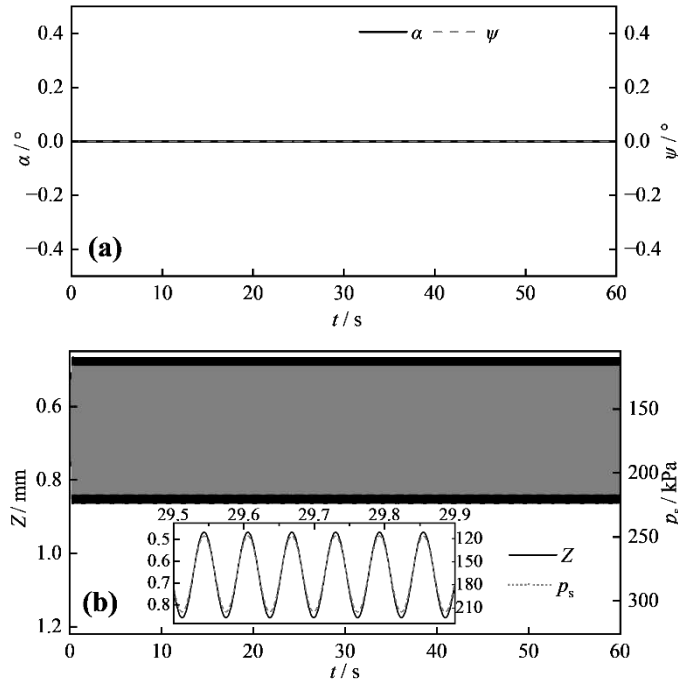
Parameters	Symbols	Units	Values
Inertia moments of motor shaft	J_0	kg·m ²	0.018
Number of pole pairs	p	-	2
Rated power	P_N	W	1 100
Rated rotational speed	n_N	rpm	1 462
Rated torque	T_N	N·m	7.18
Rated frequency	f_N	Hz	50 Hz
Rated slip	s_N	-	0.025 3
Motor overload coefficient	α_{MT}	-	2.5
Axis damping coefficient of the induction motor	f_i	N·m·s/rad	1×10^{-6}

406 4.2. System behavior

407 This section outlines the system's behavior when the shaker's two eccentric rotors function
408 synchronously, either maintaining or losing contact between the base of shaker and the foundation

409 surface. It then examines a potential scenario where the rotors rotate asynchronously while the base
410 stays in contact with the foundation. These classical cases are presented primarily to study the
411 relationship between the eccentric rotor's phase difference and the shaker's operating state.

412 Fig. 9 shows the vibrating system's dynamic behavior under the conditions: $k_f=251.0$ MPa/m,
413 $c_f=868.3$ kPa·s/m, $n_s=200$, $n_e=1$, $f=32$ Hz, along with two equal-weight eccentric rotors in the
414 simulation. Initial conditions are $\varphi_1=\varphi_2=-90^\circ$, denoting the eccentric rotors' alignment beneath the
415 motor shaft, and $\psi=0$, indicating a level foundation surface. Fig. 9a demonstrates that the phase
416 difference α between the dual eccentric rotors calculated by $\varphi_1-\varphi_2$ remains invariant at zero, thereby
417 ensuring synchronized rotation. This synchronicity leads to the generation of forces exclusively in the
418 vertical direction, nullifying any horizontal force components. Further, the shaker displacement along
419 the ψ -axis remains negligible, as confirmed by Fig. 9a. Fig. 9b which shows synchronized rotation
420 elicits a vertical dynamic displacement Z ranging from 0.47 mm to 0.86 mm, correlating with stress p_s
421 on the foundation under the loading plate of between 117 and 216 kPa. p_s is calculated as the total
422 force at the base of the loading plate divided by its bottom area. This total force is determined by
423 summing the products of vertical displacement and stiffness (k_f) per unit area within the contact area
424 between loading plate and ground. The persistent positive displacement and uninterrupted soil loading
425 confirm no detachment of the shaker base from the foundation. It is important to note that the black or
426 grey regions depicted in Fig. 9b and other similar illustrations represent tightly bunched cycles.
427 Detailed cycle traces are seen in the magnified sections within the figure.



428

429

430

Fig. 9. System behavior of ground-attached shaker with eccentric rotors synchronization: (a) α and ψ ; (b) Z and p_s .

431

Changing n_e to 5, as based on the system configuration of Fig. 9, yields the dynamic response depicted

432

in Fig. 10. Fig. 10a confirms continuous synchronized rotation of the eccentric rotors, negating any ψ -

433

direction displacement. Fig. 10b shows that Z spans from -1.50 mm to 2.17 mm, corresponding to p_s

434

ranging from 0 to 540 kPa. The augmented rotor mass amplifies the dynamic excitations, thereby

435

broadening the range of both displacement and stress in Fig. 9b. Notably, the negative minimum

436

displacement and null stress signify that detachment of the shaker base from the foundation occurs

437

during the shaker's operation. In addition, the contact state between the shaker and foundation is

438

determined by the combined effects of the Z - and ψ -directed motions. However, a minima of zero for

439

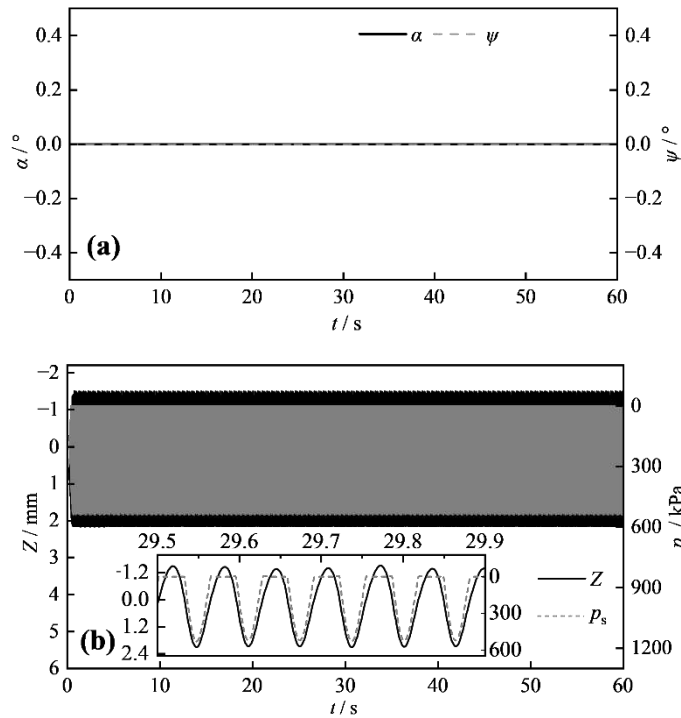
a single parameter p_s can serve as a definitive indicator of their detachment. Consequently, checking

440

whether p_s is less than zero provides a straightforward method to ascertain whether the shaker is

441

detached from the ground.



442

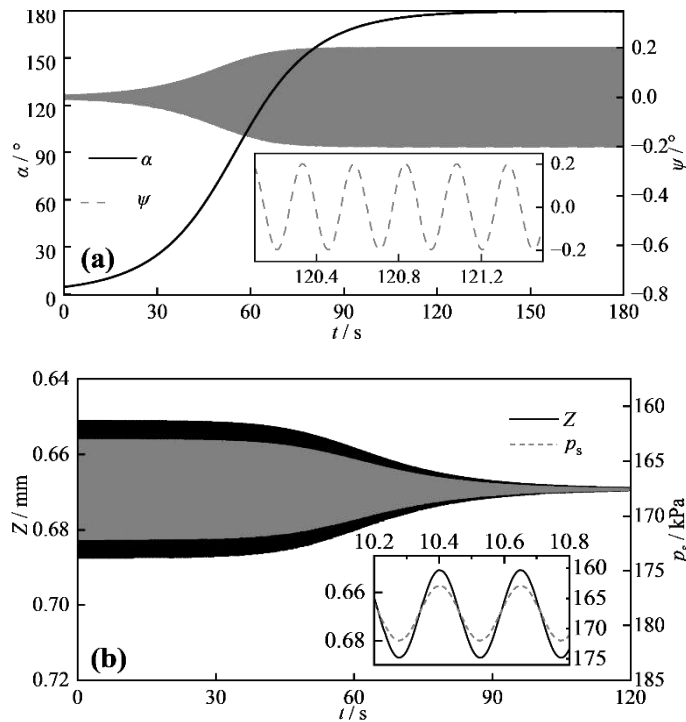
443

444 **Fig. 10.** System behavior of detached shaker with eccentric rotors synchronization: (a) α and ψ ; (b) Z and p_s .

445 Changing n_e to 3 and f to 8 Hz, based on the Fig. 9 setup, and with initial conditions $\varphi_1 = -88^\circ$ and
 446 $\varphi_2 = -92^\circ$, produces the dynamic profile in Fig. 11. Fig. 11a unveils a gradual escalation of the phase
 447 difference α , stabilizing at 180° . At this phase difference, the vertical and horizontal force components
 448 generated by each rotor cumulatively yield torques about the shaker's centroid. These torques induce
 449 rotational displacements in the ψ -direction, swinging between approximately -0.2° and 0.2° . If the
 450 excitation from the eccentric rotor is significantly amplified, desynchronization may induce substantial
 451 rotational displacements in the shaker, thereby elevating the risk of equipment tipping. Concurrently,
 452 α at 180° nullifies the vertical net force from the rotor excitations, culminating in Z and p_s of
 453 approximately 0.67 mm and 168 kPa, respectively—values in alignment with the corresponding values
 454 due to shaker's self-weight, as shown in Fig. 11b. Analysis of the shaker's dynamic behavior under
 455 these three operating conditions suggested that the mechanical design was likely effective for testing

456 railway earthworks, provided that the shaker's two eccentric rotors were synchronized and the shaker
 457 remains grounded during operation.

458



459

460 **Fig. 11.** System behavior during asynchronous rotation of eccentric rotors: (a) α and ψ ; (b) Z and p_s .

461 4.3. Analysis of shaker performance under varied initial conditions

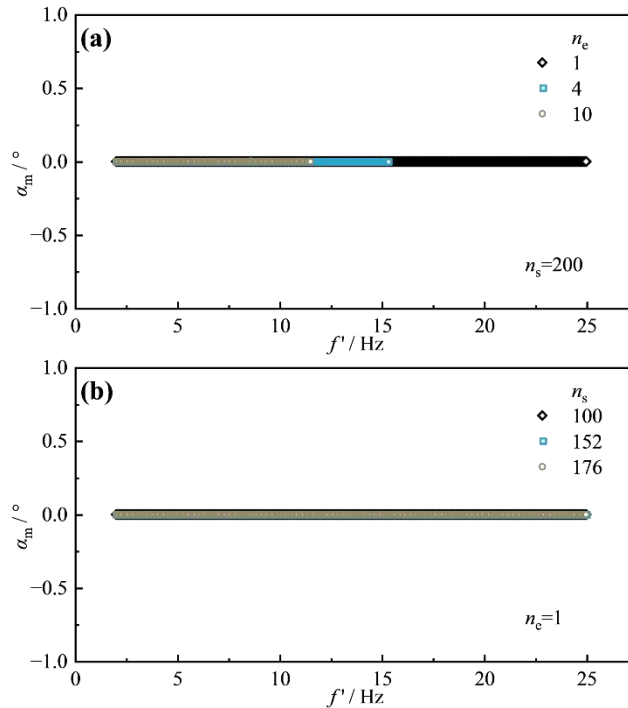
462 This section first examines the synchronization of the two eccentric rotors in the shaker under ideal
 463 conditions. However, field conditions may differ from the ideal conditions when applying to in-situ
 464 earthworks. Therefore, this section also analyses the effect of three variables: an initial phase difference
 465 in the eccentric rotors, inclined earthwork surfaces, and mass disparities in the shaker eccentric blocks.
 466 The foundation for all tests is characterized by k_f of 251.0 MPa/m and c_f of 868.3 kPa·s/m.

467 4.3.1 Ideal conditions

468 Fig. 12 presents the variation in the maximum absolute value of phase difference α_m of the eccentric
 469 rotors with respect to the motors' rotational frequency f' under ideal conditions. These observations

470 are based on the last few tens of cycles during 180 s of operation when the shaker stays in contact with
 471 the ground. A larger α_m suggests reduced capacity for the eccentric rotor to sustain synchronous
 472 rotation in the given configuration. Here, ideal conditions refer to $\varphi_1=\varphi_2=-90^\circ$ initially, $m_1=m_2$, and a
 473 horizontal foundation surface. In Fig. 12a, when $n_s=200$ and $n_e=1$, the maximum f' for the contact
 474 between shaker and foundation is 25 Hz. Increasing n_e to 4 and 10 results in a higher force due to
 475 increased rotor mass, which in turn lowers the maximum f' for the shaker in contact with the foundation
 476 to approximately 15.3 Hz and 11.5 Hz, respectively. Fig. 12b focuses on a configuration with $n_e=1$ and
 477 varying n_s values of 100, 152, and 176. The shaker remains attached to the ground. Importantly, under
 478 the ideal conditions illustrated in Fig. 12, the phase difference of the eccentric rotors consistently
 479 remains at zero, thereby sustaining synchronous operation.

480



481

482

Fig. 12. Ideal operational state influences: (a) effect of n_e ; (b) effect of n_s .

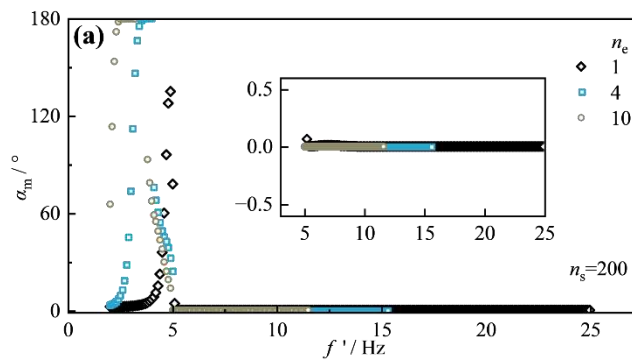
483

4.3.2 Initial rotor phase difference

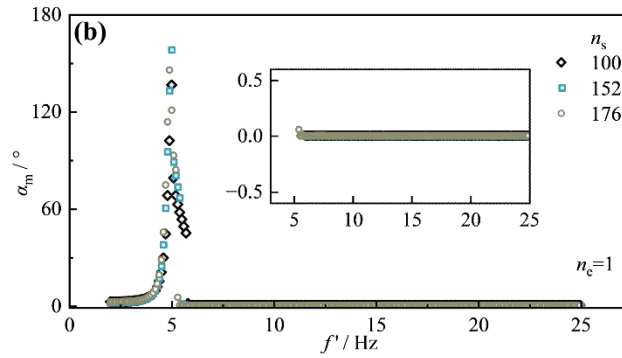
484

Under initial conditions, the center of mass of the eccentric rotor may not align vertically with the

485 motor shaft, posing challenges for precise adjustment. This scenario can be quantified in the dynamic
486 model by considering an initial phase difference between the eccentric rotors. Based on the ideal
487 condition, the initial phases of these rotors, represented as φ_1 and φ_2 , are configured at -89° and -91° ,
488 respectively. The impact of a 2° initial phase difference on the relationship between α_m and f' is
489 illustrated in Fig. 13. A comparison between Fig. 13 and Fig. 12 reveals that a minor initial phase
490 difference does not affect the maximum f' for the contact between shaker and foundation. However, if
491 f' falls below the natural frequency of 5.11 Hz associated with ψ -directed motion, α_m is magnified
492 substantially, as shown in Fig. 13a. This indicates a poor synchronization of rotors. When f' is greater
493 than 5.11 Hz, the system can adjust the phase difference to zero, thereby achieving automatic
494 synchronization. Decreasing n_s to values of 100, 152, and 176, the natural frequency in ψ -directed
495 motion increases to 5.79 Hz, 5.49 Hz, and 5.32 Hz, respectively. The variation in α_m for $n_e=1$ as a
496 function of f' is depicted in Fig. 13b. This graph also indicates that self-synchronization of rotors is
497 poor when f' is below the natural frequency related to ψ -directed motion. In conditions involving other
498 frequencies, the system manages to nullify the phase difference of eccentric rotors.



499



500

501

Fig. 13. Operational state with initial rotor phase difference: (a) effect of n_e ; (b) effect of n_s .

502

4.3.3 Earthwork inclination

503

In the idealized condition, ψ was set to 0.5° initially to mimic an experimental scenario where the

504

shaker's foundation surface exhibited a minor inclination. Fig. 14 illustrates how α_m varies with f'

505

under these conditions of a slightly tilted foundation surface. A comparison between Fig. 14 and Fig.

506

12 reveals this minor inclination does not influence the maximum value of f' for the contact between

507

shaker and foundation. Likewise, the phase difference between the two eccentric rotors is difficult to

508

stabilize near a value of 0 when f' is below the natural frequency associated with ψ -directed motion,

509

as shown in Fig. 14a. For a configuration where $n_e=1$, Fig. 14b presents the variation of α_m with f'

510

when n_s sequentially decreases to 176, 152, and 100. The results indicate the eccentric rotors operate

511

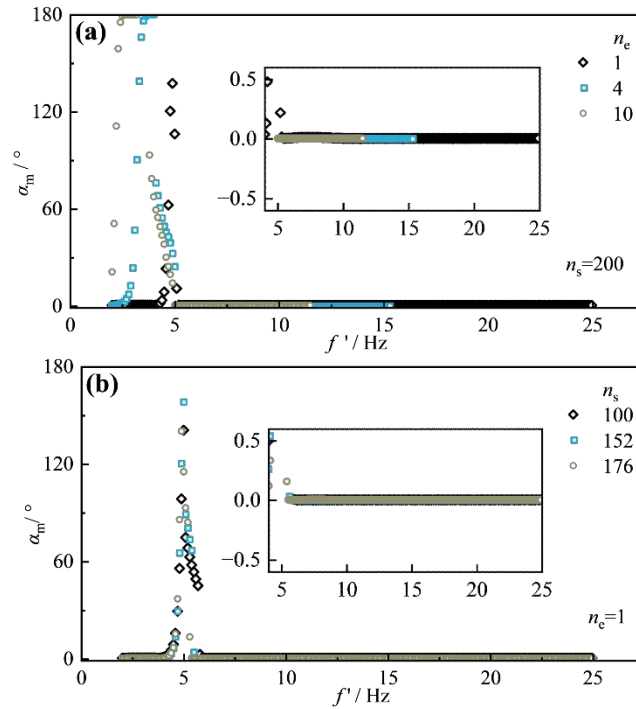
asynchronously when f' is marginally less than the natural frequency linked to ψ -directed motion.

512

However, once f' decreases to approximately 4 Hz or lower, the rotor phase difference stabilizes close

513

to 0, implying synchronisation.



514

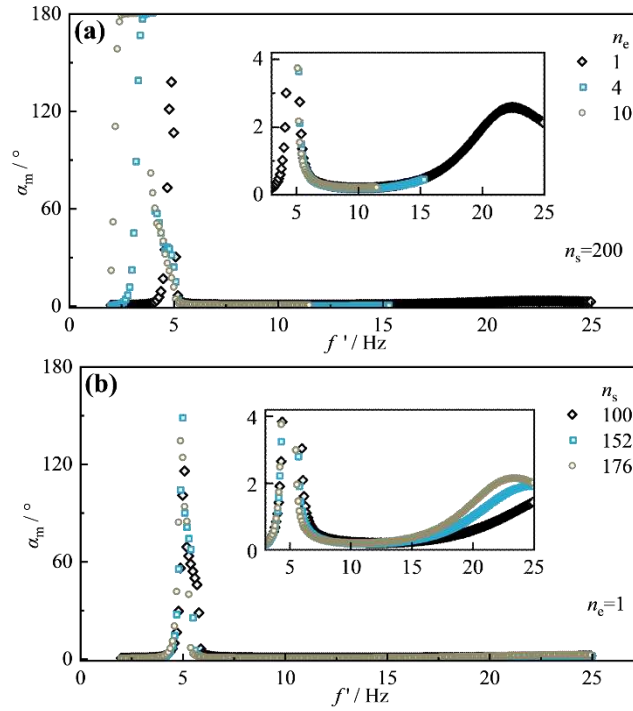
515

516 **Fig. 14.** Operational state on an inclined foundation: (a) effect of n_e ; (b) effect of n_s .

517 **4.3.4 Shaker mass discrepancies**

518 Due to variations in machining accuracy, the dimensions of eccentric blocks can differ, leading to
 519 discrepancies in their mass. Under ideal conditions, the standard masses of the eccentric rotors, m_1 and
 520 m_2 , were adjusted by -1.5% and $+1.5\%$ to account for these mass differences. Fig. 15 illustrates how
 521 α_m varies with f' when the masses of two eccentric rotors differ. A comparison of Fig. 15 with Fig. 12
 522 reveals that mass discrepancies in the eccentric rotors do not affect the maximum value of f' without
 523 the shaker being detached from the foundation. However, small mass differences induce varying phase
 524 differences in the eccentric rotors, as shown in Fig. 15a. When f' is near or below the natural frequency
 525 associated with the shaker's ψ -directed motion, α_m is significantly larger, implying the phase difference
 526 of the eccentric rotors develops most rapidly. Conversely, if f' exceeds this natural frequency, α_m
 527 remains small, indicating the eccentric rotors are approximately synchronous. Specifically, the smallest
 528 values of α_m occur when f' ranges between 6 Hz and 17 Hz. In the simulations corresponding to $n_e=1$

529 in Fig. 15a, varying n_s to 100, 152, and 176 respectively yielded the impact of f' on α_m as depicted in
 530 Fig. 15b. Similarly, it has been observed that α_m exhibits a notable increase when f' is marginally
 531 below the natural frequency associated with ψ -directed motion.



532

533
534

535 **Fig. 15.** Operational state with rotor mass discrepancies: (a) effect of n_c ; (b) effect of n_s .

536 The simulations conducted in this section demonstrate the efficacy of the shaker design under idealized
 537 conditions. Moreover, these simulations indicated the mechanical design's potential applicability in
 538 non-idealized field conditions at frequencies f' above natural frequency linked to ψ -directed motion.

539 5. Field testing

540 This section begins with an overview of the shaker's manufacture. It then details a field calibration test
 541 on strongly weathered red-bed mudstone, aimed at assessing the shaker's performance across different
 542 configurations. Additionally, a method is introduced for estimating stiffness and damping coefficients
 543 in earthworks. Following this, an analysis of the test data in conjunction with simulations is provided.

544 It then concludes with a method for designing shaker configurations based on required loads.

545 5.1. Shaker manufacture

546 The components of the shaker depicted in Fig. 16 were machined according to the design illustrated in
547 Fig. 7. The motors shown in Fig. 16a were secured using double rows of bolts on the internal frame
548 positioned on the inside of the external frame in Fig. 16b. The double-layered circular loading plate,
549 presented in Fig. 16c and d, was affixed to the bottom of the inner frame. During the experiments, the
550 motor's power supply frequency was regulated using a frequency modulator depicted in Fig. 16e,
551 connected to a 380 V, 50 Hz source. Additionally, Fig. 16f illustrates counterweight blocks, and Fig.
552 16g shows an eccentric block.

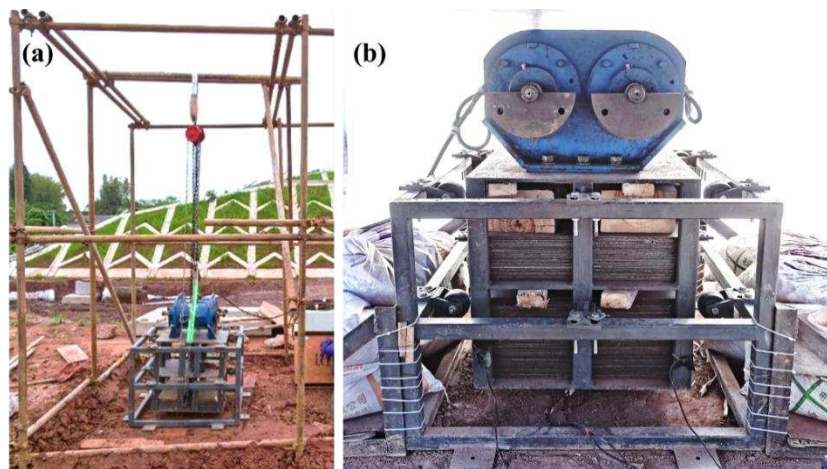


553
554 **Fig. 16.** Shaker components: (a) motors; (b) internal and external frame; (c) top view of the loading plate; (d) side
555 view of loading plate; (e) frequency modulator; (f) counterweight blocks; (g) eccentric block.

556 5.2. Site condition and shaker setup

557 A calibration test was conducted near a railway line under construction, with earthworks consisting of

558 strongly weathered red-bed mudstone. The strongly weathered mudstone in the vicinity of the test
559 location had a upper crust thickness ranging from 10 to 13 cm, a density of 2080 kg/m³, and a moisture
560 content between 6.2% and 10.4%. Additional properties included a modulus of subgrade reaction (K_{30})
561 ranging from 93.4 to 138.2 MPa/m and a saturated permeability coefficient of approximately 8.59×10^{-5}
562 cm/s at a temperature of 20 °C. Beneath this crust lay weakly weathered red-bed mudstone. Fig. 17
563 illustrates the shaker during the in-situ calibration test. As depicted in Fig. 17a, a support structure,
564 crafted from steel tubes, was erected to suspend a hoisting block. This block facilitated the lifting and
565 positional adjustment of the shaker. Fig. 17b presents the fully assembled shaker. To inhibit relative
566 displacement between the counterweights and the inner frame, wooden blocks were inserted into the
567 gap.



568
569 **Fig. 17.** Shaker at the test site: (a) shaker and lifting frames; (b) assembled shaker.

570 In the test, a force measurement system as depicted in Fig. 18 was employed to quantify the load
571 exerted on the earthworks. This system includes a force-measuring device as shown in Fig. 18a and
572 Fig. 18b, positioned between the loading plate and the ground, as well as a data acquisition instrument
573 manufactured by the imc Test and Measurement GmbH and a microcomputer in Fig. 18c. The force-

574 measuring device incorporates three load cells, evenly spaced at 120° intervals between two circular
575 steel plates. These plates have a diameter of 300 mm and a thickness of 10 mm. The load cells, of type
576 “QLMH-P”, have specifications: height of 30 mm, diameter of 58 mm, capacity range of 2 t, accuracy
577 of 0.3% F.S. (full scale), resolution of 0.1% F.S., and sensitivity of 2.0 mV/V. These load cells interface
578 with the imc data collector and microcomputer to record the applied load from the shaker to the
579 foundation. Prior to testing, the soil surface beneath the force-measuring device was leveled using sand,
580 as shown in Fig. 18d.



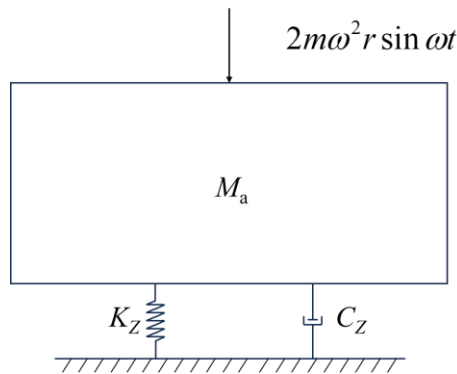
581
582 **Fig. 18.** Force measurement system: (a) force-measuring device; (b) load cell configuration; (c) microcomputer and
583 data acquisition instrument; (d) site levelling.

584 In the experiment, adjustments were made to the number of counterweight blocks (n_s), setting them
585 sequentially to 100, 152, and 200. The number of eccentric blocks (n_e) at each motor end was set to 1,
586 2, 3, 4, 7, and 10 in sequence. Frequency sweep tests were conducted by incrementally enlarging the
587 supply frequency (f) from 2 to 50 Hz for each combination of n_s and n_e . Observe the output load
588 waveform on the microcomputer in real time. Following a period of stabilization of the shaker's output
589 at the current frequency, adjust the frequency to the next level, with an increment of approximately 2.0
590 Hz. During actual operation, the equipment's operating status was also continuously monitored and a
591 kill switch was available if the equipment showed signs of tipping or jumping.

592 **5.3. Parameters estimation**

593 Stiffness and damping of earthworks are important for analyzing the dynamic response of track-
 594 foundation systems under train loading [1,7,8]. Here, a straightforward method for estimating the
 595 stiffness coefficients (K_Z) and damping coefficients (C_Z) of soil based on field test data is proposed.

596 In cases of suboptimal synchronization between the eccentric rotors, the exciting force—measured
 597 when their phase difference has not fully developed—is regarded as the shaker's output. Under this
 598 condition, the two eccentric rotors rotate nearly in sync, allowing the shaker to ignore swing. Assuming
 599 equal mass for the eccentric rotors ($m_1=m_2=m$), the shaker model simplifies to a damped vibration
 600 system with single degree of freedom. This system is excited by a simple harmonic load, as depicted
 601 in Fig. 19, for which an analytical solution exists.



602
 603 **Fig. 19.** Simplified vibration system diagram.

604 The stresses transmitted from the shaker to the underlying foundation comply with Eq. (36):

$$605 \begin{cases} p_{p,v} = (M_a g \pm 2\beta_a m\omega^2 r) / (\pi r_b^2) \\ p_{p-v} = 4\beta_a m\omega^2 r / (\pi r_b^2) \end{cases} \quad (36)$$

606 where p_p and p_v indicate the maximum and minimum values of the time-range curve of the stress
 607 exerted on the foundation by the shaker's loading plate, respectively. $\omega=2\pi f'$ represents the angular
 608 frequency of the eccentric rotors. The peak-to-valley stress values, denoted as p_{p-v} , which indicate the
 609 difference between p_p and p_v , should not be greater than $2M_ag/(\pi r_b^2)$. The amplification factor, β_a , is

610 analytically defined by Eq. (37):

$$611 \quad \beta_a = \frac{1}{\sqrt{\left[1 - \left(\frac{\omega}{\sqrt{K_Z / M_a}}\right)^2\right]^2 + \left(\frac{\omega C_Z}{K_Z}\right)^2}} \quad (37)$$

612 If the vibration of the shaker in the situ test is expressed as Fig. 19, both m and M_a in model can be
613 measured using scales. The value of r is derived from the eccentric block's geometry, while ω is
614 determined by the supply frequency. The variables K_Z and C_Z remain the only unknowns. However,
615 the experimental relationship between β_a and ω can be derived from frequency-sweep vibration tests
616 with shaker under specific configurations. The test value of β_a was determined as the ratio between the
617 peak-to-valley value of the combined force measured beneath the loading plate and $4m\omega^2r$. Moreover,
618 Eq. (37) analytically expresses β_a , correlating it with ω , M_a , K_Z and C_Z . By keeping M_a consistent with
619 test conditions, the analytical β_a - ω curves for certain set of K_Z and C_Z values may depict its
620 experimental relationship. Optimization algorithms can be employed to find K_Z and C_Z values that best
621 match the measured β_a - ω relationship, thereby defining the foundation's stiffness and damping
622 coefficients. The objective function is determined as the coefficient of determination (R^2), indicating
623 better agreement between the analytical and measured β_a - ω relationship as it approaches 1.0. Then,
624 estimating the earthwork's stiffness and damping transforms into a mathematical challenge of
625 identifying K_Z and C_Z values that maximize R^2 as calculated from Eq. (38) [42]:

$$626 \quad R^2 = 1 - \frac{\sum_{i=1}^N (\beta_{a,i} - \hat{\beta}_{a,i}(K_Z, C_Z))^2}{\sum_{i=1}^N (\bar{\beta}_{a,i} - \hat{\beta}_{a,i}(K_Z, C_Z))^2} \quad (38)$$

627 where N denotes the number of samples of the data; $\beta_{a,i}$ represents the test value; $\hat{\beta}_{a,i}(K_Z, C_Z)$
628 denotes the estimated value determined using Eq. (37); $\bar{\beta}_{a,i}$ is the mean of the measured values.

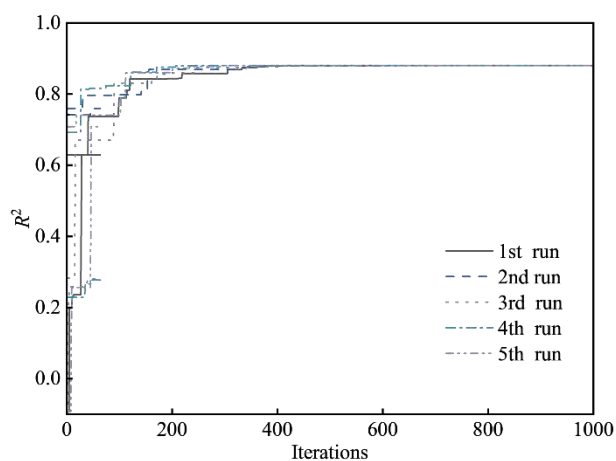
629 Table 3 presents a set of test data for β_a and ω , as determined through frequency sweep tests on

630 highly weathered red bedded mudstone. These tests used shaker settings of $n_s=200$ and $n_e=2$, yielding
631 a M_a of 1205.3 kg. To derive the values for K_Z and C_Z , the flower pollination algorithm (FPA) [43,44]
632 was applied, using data from Table 3. Key parameters for the FPA included a switch probability of 0.8,
633 a population size of 20, and a scaling factor of 1×10^{-5} for the Lévy flight step size.

634 **Table 3.** The measured βa - ω relationship

f (Hz)	ω (rad/s)	βa	f (Hz)	ω (rad/s)	βa	f (Hz)	ω (rad/s)	βa	f (Hz)	ω (rad/s)	βa
8.07	25.35	1.07	20.16	63.33	1.19	31.83	100.00	2.01	46.25	145.30	1.47
10.18	31.98	1.11	22.20	69.74	1.22	34.08	107.07	2.43	46.55	146.24	1.38
11.94	37.51	1.11	24.14	75.84	1.29	36.02	113.16	2.59	48.50	152.37	1.30
14.12	44.36	1.07	26.10	82.00	1.35	40.56	127.42	2.10	50.00	157.08	1.07
16.24	51.02	1.23	28.16	88.47	1.48	42.50	133.52	1.84			
18.04	56.67	1.18	30.09	94.53	1.64	44.80	140.74	1.60			

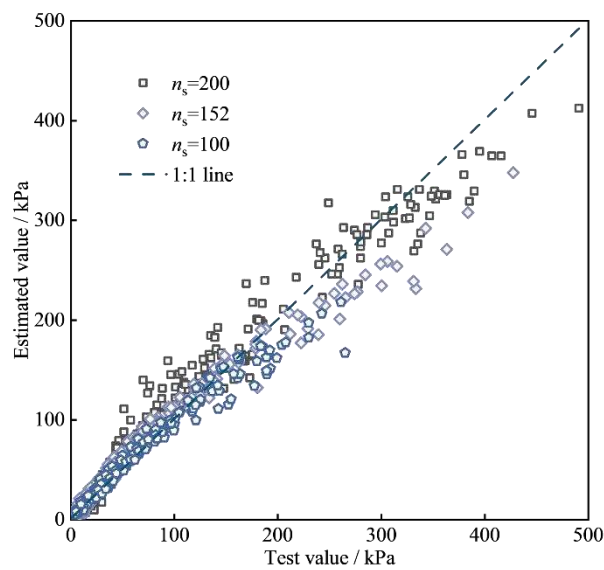
635 Fig. 20 displays the iteration history of R^2 across five runs of FPA, revealing that the algorithm obtains
636 a maximum R^2 value of 0.88 after less than 500 iterations. The values of K_Z and C_Z obtained from five
637 runs show strong consistency after 1000 iterations. The mean values suggest K_Z and C_Z were 17.7
638 MN/m and 61.4 kN·s/m, respectively. In addition, according to Eq. (1), under the condition that the
639 loading plate of the shaker is not separated from the ground, the resulting K_Z and C_Z ratios to the
640 loading plate's bottom area represent the per unit area stiffness and damping, denoted by k_f and c_f ,
641 respectively. k_f is calculated at 251.0 MPa/m and c_f at 868.3 kPa·s/m.



642

643 **Fig. 20.** Iteration histories of R^2 .

644 The ease and accuracy of the shaker's self-weight calculation allow for checking the suitability of Eq.
645 (36) in estimating the shaker's output via verifying the p_{p-v} equation. Additionally, p_{p-v} correlates with
646 β_a , which is derived from K_Z and C_Z , among others. Therefore, this process also verifies the validity of
647 the K_Z and C_Z values derived from the estimation. Fig. 21 presents a comparison of the tested and
648 estimated values of p_{p-v} derived from various conditions, characterized by differing values of n_s and n_e
649 in frequency sweep test. It is observed that the estimated values are marginally lower than the tested
650 values at higher load values. Overall, the data points are closely aligned with the 1:1 line,
651 demonstrating a significant consistency between the estimated and experimental values. This
652 alignment substantiates the reliability of Eq. (36) and the estimation method used for K_Z and C_Z .

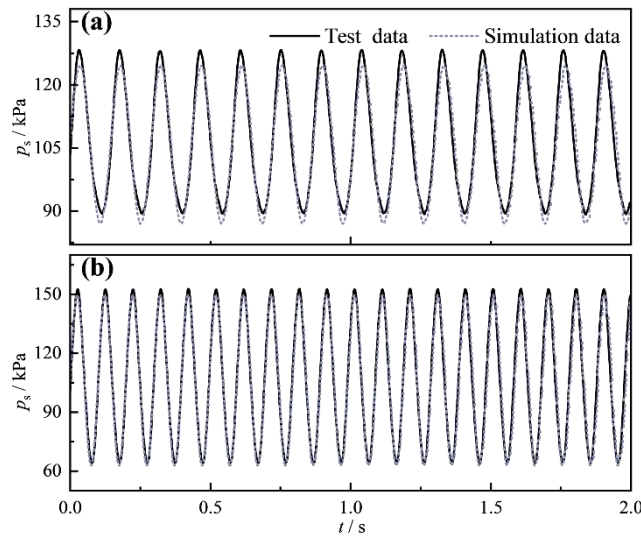


653
654 **Fig. 21.** Estimated vs. measured p_{p-v} comparison.

655 **5.4. Results and interpretation**

656 Fig. 22 presents the time-history of stress p_s exerted on the foundation surface by the shaker during the
657 system's stable phase. The time variable (t) depicted in the figures signifies the relative time difference

658 rather than the actual operational duration of the system. In Fig. 22a, with $n_s=100$, $n_e=4$, and supply
659 frequency f of 13.84 Hz, the maximum value of p_s reaches approximately 125 kPa, while the minima
660 is approximately 90 kPa. The corresponding loading frequency is approximately 7 Hz. The discrepancy
661 between the simulation and experimental data for the maximum and minimum values of p_s remains
662 within a 5% margin, and the frequencies are essentially identical. Alternatively, for f of 20.19 Hz, the
663 time-dependent profile of p_s is depicted in Fig. 22b. The maximum and minimum values of p_s are
664 approximately 150 kPa and 64 kPa, respectively, with f' approximately 10 Hz. Once again, the
665 simulation data aligns well with the experimental findings.

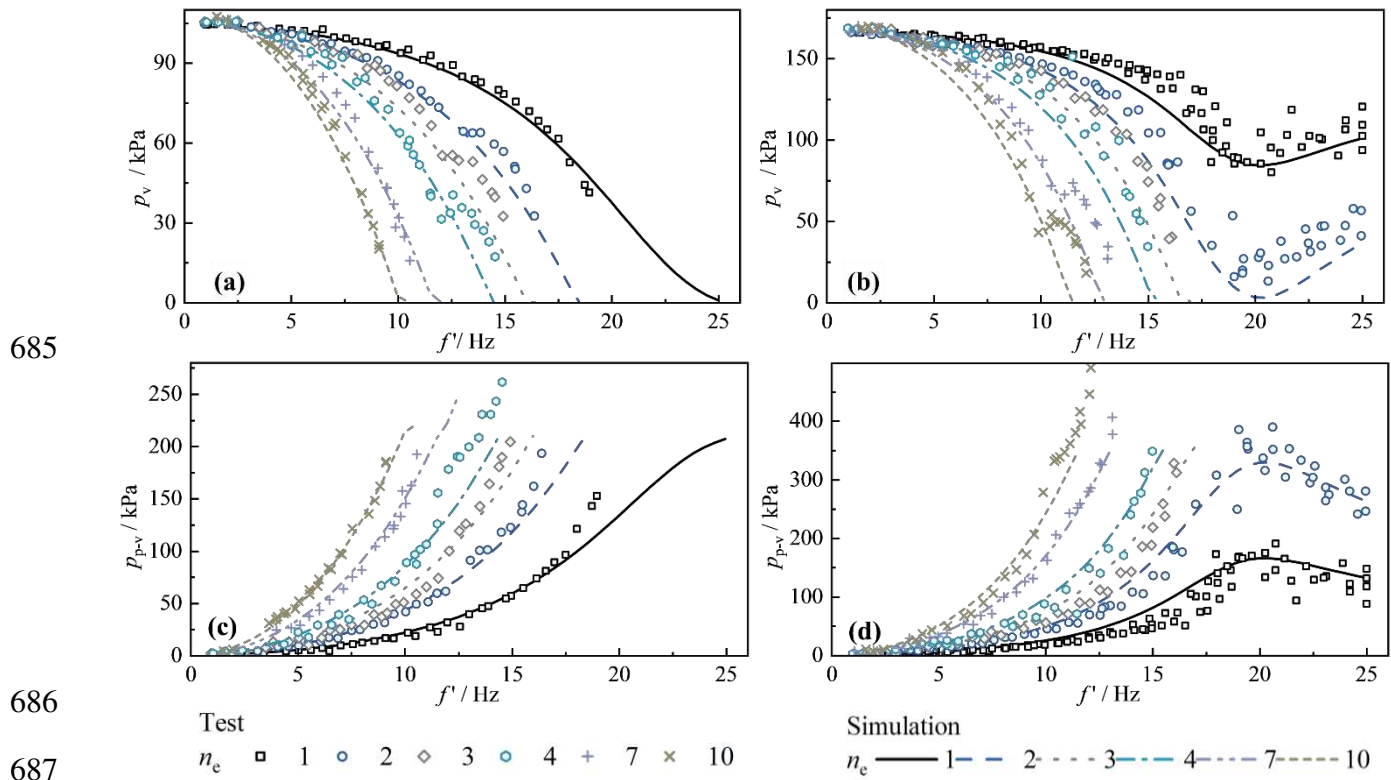


666

667 **Fig. 22.** Time-dependent stress response analysis: (a) $n_s=100$, $n_e=4$, $f=13.84$ Hz; (b) $n_s=100$, $n_e=4$, $f=20.19$ Hz.

668 The experimental test data and simulation data of stresses applied to the foundation surface by the
669 shaker with varying n_s and n_e are compared in Fig. 23. The data in these figures pertain to conditions
670 where the shaker remains attached to the foundation. Data pertaining to certain conditions involving
671 poorly synchronized eccentric rotors were obtained during intervals when the phase difference between
672 the two rotors had not yet fully evolved. Fig. 23a illustrates the relationship between the stress minima

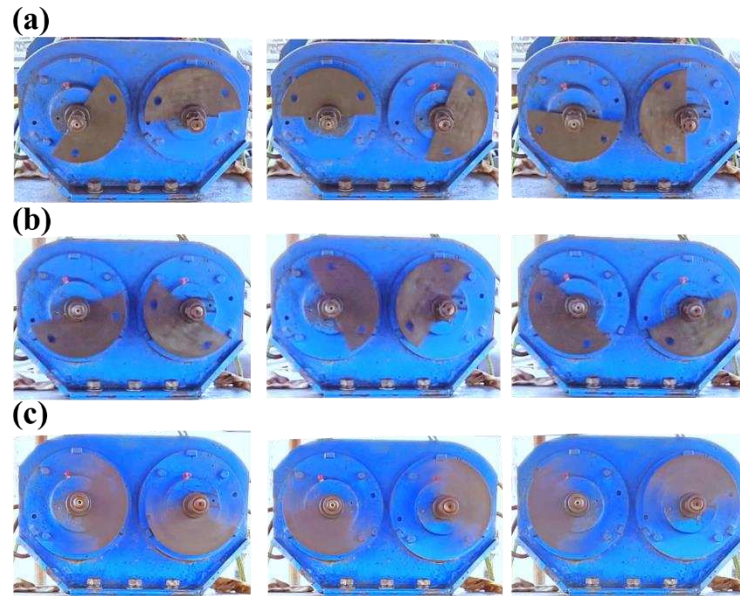
673 (p_v) and the eccentric rotors' rotation frequency (f') for varying n_e with n_s set at 100. For Z-directed
674 motion, the natural frequency of the system is approximately 24.48 Hz. Typically, f' is lower than this
675 natural frequency. As f' or n_e increases, the excitation from the rotating eccentric rotors intensifies,
676 resulting in a decrease in p_v . The simulated and field values of p_v exhibit strong consistency. The
677 experimental maximum value of f' in scenarios where the shaker is in constant contact with foundation
678 is marginally smaller than the simulated value. This discrepancy can be attributed to the early
679 termination of the test, which was necessitated by instability issues arising from an inadequate shaker
680 counterweight as p_v approached zero. When n_s is adjusted to 200, Fig. 23b displays the correlation
681 between p_v and f' . Again, a strong correlation between simulated and experimental data is observed.
682 It can also be observed that the trend of p_v shifts from decreasing to increasing as f' increases for
683 configurations where n_e is either 1 or 2 and f' exceeds the natural frequency for Z-directed motion
684 (approximately 19.34 Hz).



688 **Fig. 23.** Foundation stress profiles by shaker: (a) p_v at $n_s=100$; (b) p_v at $n_s=200$; (c) p_{p-v} at $n_s=100$; (d) p_{p-v} at $n_s=200$

689 Fig. 23c and Fig. 23d illustrate the relationship between peak-to-valley values (p_{p-v}) of stress and
690 rotation frequency (f') of eccentric rotors for n_s of 100 and 200, respectively. When f' is lower than
691 the natural frequency, an increase in f' or n_e amplifies the excitation generated by the eccentric rotors'
692 rotation, subsequently increasing p_{p-v} . Conversely, when f' exceeds the natural frequency, p_{p-v} reduces
693 as f' increases. Furthermore, Fig. 23c and Fig. 23d also confirm the close alignment between simulated
694 and experimental p_{p-v} values.

695 The phases of the eccentric rotors considering $n_s=200$ and $n_e=1$ are depicted in Fig. 24. During
696 several moments corresponding to $f'=3.52$ Hz in Fig. 24a, the eccentric rotors demonstrate
697 asynchronous operation. Concurrently, the shaker exhibits swinging behavior that aligns with the
698 direction of ψ in the aforementioned mathematical model. Contrastingly, at $f'=12.36$ Hz, shown in Fig.
699 24b, the phases of the eccentric rotors appear consistent. Under these conditions, the shaker operates
700 without swinging. However, poor synchronization of the eccentric rotors occurs again at $f'=23.40$ Hz,
701 as indicated in Fig. 24c, accompanied by a minor swing in the shaker. Of particular note is the
702 significant swing of the shaker when f' approaches 5 Hz. Under these conditions the experiment was
703 terminated to prevent equipment tipping. Alternatively, the supply frequency should be rapidly
704 elevated before the phase difference of the eccentric rotors is sufficiently developed. Moreover,
705 observations from experimental phenomena indicate optimal stable operation of the shaker occurs
706 when eccentric rotors' rotational frequency f' lies within the range of approximately 6 to 16 Hz. These
707 observations align with the simulation analysis presented in Section 4.3.



708

709 **Fig. 24.** Eccentric block phasing at differing frequencies: (a) $f'= 3.52$ Hz; (b) $f'=12.36$ Hz; (c) $f'=23.40$ Hz.

710 **5.5. Configuration design**

711 To enhance experimental efficiency and reduce the costs of sensor usage in the cumulative settlement
 712 test over a long period of time, it is suggested to conduct frequency sweep tests on the earthworks to
 713 be evaluated. These tests serve the purpose of assessing the stiffness and damping properties of the
 714 earthworks, providing estimations for the shaker's output load without the use of load cells.
 715 Subsequently, the shaker configuration can be adjusted to produce the requisite force according to the
 716 output stress characteristics. This process determines shaker configuration including the number of
 717 eccentric blocks (n_e) at each end of the shaker motor, the total count of counterweight blocks (n_s), and
 718 the supply frequency (f). Output stress characteristics determined by train loading include the
 719 minimum value (p_v), the peak-to-valley value (p_{p-v}) and the frequency. The frequency could be
 720 regarded as the rotational frequency (f') of the motors. The procedure of configuration design is
 721 illustrated in Fig. 25 and consists of the following steps:

722

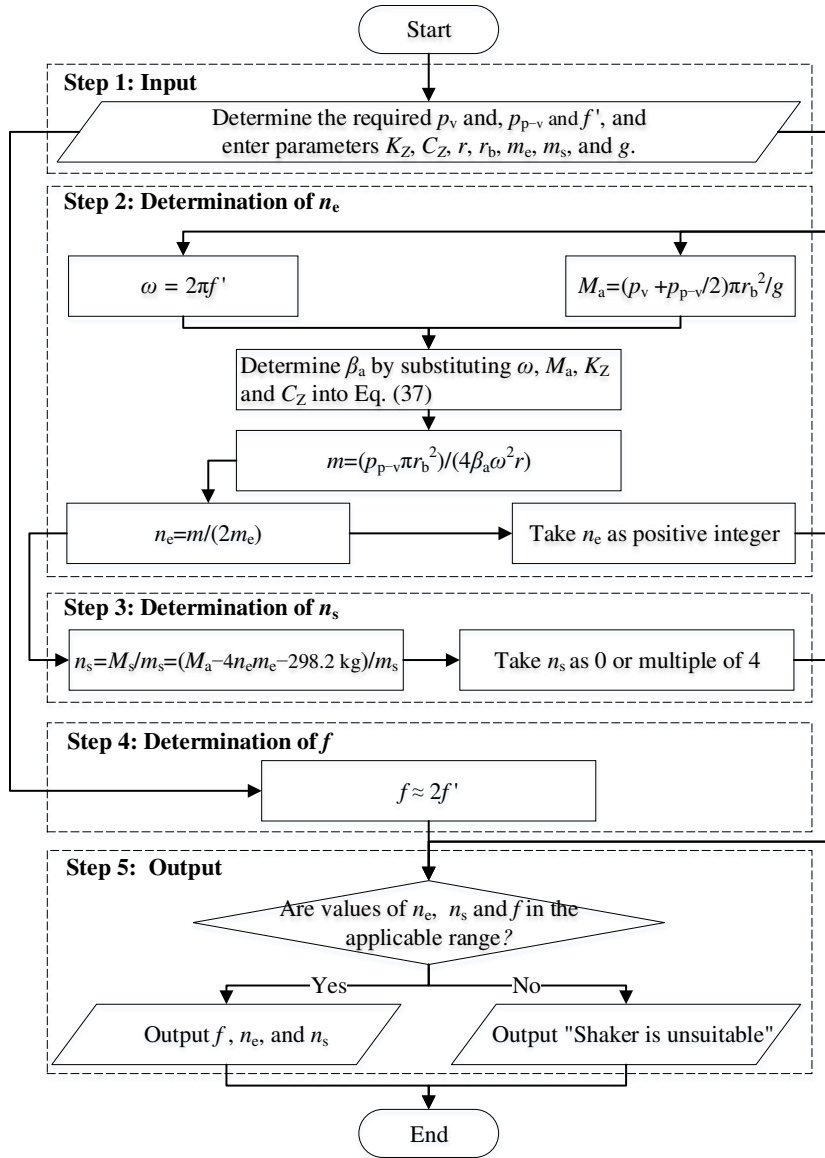
723 **Step 1: Input.** Specify the desired stress characteristics p_v , p_{p-v} , and f' , along with other known
724 parameters such as K_Z , C_Z , r , r_b , m_e , m_s , and g .

725 **Step 2: Determination of n_e .** After calculating ω and M_a from the provided parameters, the
726 amplification factor (β_a) is derived from Eq. (37). Subsequently, the desired value of n_e is obtained
727 from the second equation in Eq. (36) and Eq. (17). Notably, n_e should be adjusted to a positive integer
728 closest to the calculated value.

729 **Step 3: Determination of n_s .** By subtracting the mass of the eccentric blocks and any other masses
730 not included in the counterweight blocks from M_a , the desired mass of the counterweight blocks (M_s)
731 is established. M_s is then divided by the mass of individual counterweight blocks (m_s) to ascertain n_s .
732 For better stability of the shaker, the counterweight blocks should be stacked at the same height. Hence,
733 it is recommended to adjust n_s to a multiple of 4 closest to the calculated value.

734 **Step 4: Determination of f .** For vibration motors equipped with two pole pairs, the required supply
735 frequency f is approximately twice the value of f' .

736 **Step 5: Output.** Numerical simulation is employed to assess whether the obtained values of n_e , n_s , and
737 f fall within the applicable range of the shaker. Finally, output recommendations for configuration.



738
739

Fig. 25. Flowchart for configuration design of shaker.

740 In a site comparable to the study area, this method determined that a configuration with $n_e = 4$, $n_s = 60$,
741 and $f = 22$ Hz would produce dynamic stress ranging from 30 to 130 kPa at 11 Hz. This stress
742 magnitude approximately aligns with that experienced in ballast track foundations under train loading.
743 Furthermore, a configuration with $n_e = 1$, $n_s = 0$, and $f = 22$ Hz would produce stress values between 30
744 and 53 kPa at 11 Hz, approximately replicating the stress range of slab track foundations.

745 6. Conclusions

746 Understanding the mechanical performance of track earthworks is important for the construction,

747 operation, and maintenance of railways. To assist with this, an earthworks shaker was developed. First
748 the design requirements were outlined, followed by the development of a conceptual model to describe
749 the shaker operation. Using the model, virtual development of the shaker was undertaken to determine
750 the effect of different factors. Lastly, the shaker was constructed and tested on a railway construction
751 site. The conclusions were:

752 (1) The shaker is suitable for studying earthworks. Data from frequency sweep tests aid in
753 estimating the stiffness and damping coefficients of earthworks. Field tests on a weathered red-bed
754 mudstone with a modulus of subgrade reaction (K_{30}) ranging from 93.4 to 138.2 MPa/m showed a
755 stiffness coefficient of 251.0 MPa and damping coefficient of 868.3 kPa·s/m. Furthermore, by
756 adjusting the shaker configuration, it is possible to generate dynamic loads that mimic the stress
757 magnitudes of track foundation under train loading.

758 (2) The proposed dual-rotor shaker is a novel design compared to current railway earth dynamic
759 test shakers. Its uniqueness stems from the lack of mechanical coupling between the two eccentric
760 rotors. This eliminates the need for a cooling system to cool the connecting mechanism, thereby
761 enhancing economic efficiency in operation and maintenance.

762 (3) The phase synchronization between the shaker's two eccentric rotors is influenced by potential
763 mass discrepancies and initial conditions. Even minor deviations from these conditions may adversely
764 affect synchronization. This issue becomes particularly problematic when the rotational frequency of
765 rotors is near or below the system's natural frequency associated with swinging motion, resulting in
766 shaker oscillations. Simulations and field tests reveal that, within a rotational frequency range of 6 to
767 16 Hz, the shaker's eccentric rotors synchronize effectively, ensuring stable loading output.

768 It is important to note that the proposed shaker encounters challenges in accurately replicating the
769 stresses induced in railway earthwork by train loading. Moreover, the correlation between the
770 frequency of simple harmonic loading and train-induced loading needs to be further explored. To
771 address these shortcomings, it is advisable to establish cumulative settlement thresholds. These
772 thresholds should be defined by subjecting the inertial shaker to railway earthworks already in practical
773 use and proven to meet usage requirements. When assessing soil in railway earthworks, the settlement
774 should not exceed this threshold under the same loading conditions. Adhering to this standard allows
775 for the better application of inertial shakers in the quantitative evaluation of railway earthworks.

776 **Data availability statement**

777 All data, models, and code generated or used during the study appear in the submitted article.

778

779 **Acknowledgments**

780 This research was funded by the National Natural Science Foundation of China (Grant No. 52078435),
781 the Natural Science Foundation of Sichuan Province (Grant No. 2023NSFSC0391), the Overseas
782 Expertise Introduction Project for Discipline Innovation ("111 Project ", Grant No. B21011), and the
783 Royal Society UK (IEC\NSFC\211306). We extend our gratitude to Mr. Jianxiang Zhou for his
784 invaluable assistance during the field trials.

785

786 **References**

- 787 [1] Guo Y, Zhai W, Sun Y. A mechanical model of vehicle-slab track coupled system with differential
788 subgrade settlement. *Structural Engineering and Mechanics* 2018;66:15–25.
789 <https://doi.org/10.12989/SEM.2018.66.1.015>.
- 790 [2] Feng G, Zhang L, Luo Q, Wang T, Xie H. Monitoring the dynamic response of track formation

- 791 with retaining wall to heavy-haul train passage. *International Journal of Rail Transportation*
792 2022;1–19. <https://doi.org/10.1080/23248378.2022.2103849>.
- 793 [3] Luo Q, Fu H, Liu K, Wang T, Feng G. Monitoring of train-induced responses at asphalt support
794 layer of a high-speed ballasted track. *Construction and Building Materials* 2021;298:123909.
795 <https://doi.org/10.1016/j.conbuildmat.2021.123909>.
- 796 [4] Mei H, Leng W, Nie R, Tu R, Li Y, Dong J. Experimental research on the dynamic response
797 characteristics of the transition subgrade induced by heavy-haul train passage. *Proceedings of the*
798 *Institution of Mechanical Engineers, Part F: Journal of Rail and Rapid Transit* 2019;233:974–87.
799 <https://doi.org/10.1177/0954409718822924>.
- 800 [5] Zhai W, Wang K, Chen Z, Zhu S, Cai C, Liu G. Full-scale multi-functional test platform for
801 investigating mechanical performance of track–subgrade systems of high-speed railways. *Rail*
802 *Eng Science* 2020;28:213–31. <https://doi.org/10.1007/s40534-020-00221-y>.
- 803 [6] Indraratna B, Ngo T, Ferreira FB, Rujikiatkamjorn C, Tucho A. Large-scale testing facility for
804 heavy haul track. *Transportation Geotechnics* 2021;28:100517.
805 <https://doi.org/10.1016/j.trgeo.2021.100517>.
- 806 [7] Zhai W, Wang K, Cai C. Fundamentals of vehicle–track coupled dynamics. *Vehicle System*
807 *Dynamics* 2009;47:1349–76. <https://doi.org/10.1080/00423110802621561>.
- 808 [8] Xie H, Luo Q, Wang T, Jiang L, Connolly DP. Stochastic analysis of dynamic stress amplification
809 factors for slab track foundations. *International Journal of Rail Transportation* 2023;1–23.
810 <https://doi.org/10.1080/23248378.2023.2170286>.
- 811 [9] Cai X, Zhang Q, Wang Q, Cui X, Dong B. Effects of the subgrade differential arch on damage
812 characteristics of CRTS III slab track and vehicle dynamic response. *Construction and Building*
813 *Materials* 2022;327:126982. <https://doi.org/10.1016/j.conbuildmat.2022.126982>.
- 814 [10] Ye Q, Luo Q, Connolly DP, Wang T, Xie H, Ding H. The effect of asphaltic support layers on slab
815 track dynamics. *Soil Dynamics and Earthquake Engineering* 2023;166:107771.
816 <https://doi.org/10.1016/j.soildyn.2023.107771>.
- 817 [11] Jiang H, Li Y, Wang Y, Yao K, Yao Z, Xue Z, et al. Dynamic performance evaluation of ballastless
818 track in high-speed railways under subgrade differential settlement. *Transportation Geotechnics*
819 2022;33:100721. <https://doi.org/10.1016/j.trgeo.2022.100721>.
- 820 [12] Wang L. Vibration characterization of fully-closed high speed railway subgrade through
821 frequency: Sweeping test. *Soil Dynamics and Earthquake Engineering* 2016;88:33–44.
822 <https://doi.org/10.1016/j.soildyn.2016.05.011>.
- 823 [13] Wang L, Lei X, Liu S. Investigation of immersion influence on dynamic properties of high-speed
824 railway subgrade with semi-rigid waterproof functional layer through field-excitation testing.
825 *Can Geotech J* 2018;55:19–33. <https://doi.org/10.1139/cgj-2016-0606>.
- 826 [14] Esen AF, Woodward PK, Laghrouche O, Connolly DP. Stress distribution in reinforced railway
827 structures. *Transportation Geotechnics* 2022;32:100699.
828 <https://doi.org/10.1016/j.trgeo.2021.100699>.
- 829 [15] Marolt Čebašek T, Esen AF, Woodward PK, Laghrouche O, Connolly DP. Full scale laboratory
830 testing of ballast and concrete slab tracks under phased cyclic loading. *Transportation*
831 *Geotechnics* 2018;17:33–40. <https://doi.org/10.1016/j.trgeo.2018.08.003>.
- 832 [16] Bian X, Jiang H, Cheng C, Chen Y, Chen R, Jiang J. Full-scale model testing on a ballastless

- 833 high-speed railway under simulated train moving loads. *Soil Dynamics and Earthquake*
834 *Engineering* 2014;66:368–84. <https://doi.org/10.1016/j.soildyn.2014.08.003>.
- 835 [17] Miwa M, Yoshimura A. Study on vertical dynamic vehicle-track interactions using the TRADYS
836 test facility and computer simulation. *Computers in Railways X*, vol. 1, Prague, Czech Republic:
837 WIT Press; 2006, p. 885–94. <https://doi.org/10.2495/CR060861>.
- 838 [18] Huang J, Su Q, Liu T, Wang X. Vibration and long-term performance analysis of pile-plank-
839 supported low subgrade of ballastless track under excitation loads. *Shock and Vibration*
840 2015;2015:1–12. <https://doi.org/10.1155/2015/404627>.
- 841 [19] Efthymiou G, Vrettos C. Kinematic response of pile groups and piled rafts to a distant stationary
842 or moving harmonic load via the FEM. *Soil Dynamics and Earthquake Engineering*
843 2024;176:108264. <https://doi.org/10.1016/j.soildyn.2023.108264>.
- 844 [20] Liu H, Luo Q, El Naggar MH, Zhang L, Wang T. Centrifuge modeling of stability of embankment
845 on soft soil improved by rigid columns. *J Geotech Geoenviron Eng* 2023;149:04023069.
846 <https://doi.org/10.1061/JGGEFK.GTENG-11314>.
- 847 [21] Zhang C, Jiang G, Buzzi O, Su L. Full-scale model testing on the dynamic behaviour of weathered
848 red mudstone subgrade under railway cyclic loading. *Soils and Foundations* 2019;59:296–315.
849 <https://doi.org/10.1016/j.sandf.2018.11.007>.
- 850 [22] Cai Y, Xu L, Liu W, Shang Y, Su N, Feng D. Field Test Study on the dynamic response of the
851 cement-improved expansive soil subgrade of a heavy-haul railway. *Soil Dynamics and*
852 *Earthquake Engineering* 2020;128:105878. <https://doi.org/10.1016/j.soildyn.2019.105878>.
- 853 [23] Ye Y-S, Lou L-W, Cai D-G, Shi Y-F, Yan H-Y, Wei S-W. Mechanical properties of track-asphalt
854 concrete-subgrade bed structure system under both temperature and train loading. *Construction*
855 *and Building Materials* 2022;340:127556. <https://doi.org/10.1016/j.conbuildmat.2022.127556>.
- 856 [24] Hou Y, Peng H, Fang P, Zou M. Synchronous characteristic of three homodromy motors in
857 vibrating isolation system. *J Mech Sci Technol* 2021;35:45–60. [https://doi.org/10.1007/s12206-](https://doi.org/10.1007/s12206-020-1204-2)
858 [020-1204-2](https://doi.org/10.1007/s12206-020-1204-2).
- 859 [25] Zhang X, Yue H, Li Z, Xu J, Wen B. Stability and coupling dynamic characteristics of a vibrating
860 system with one internal degree of freedom and two vibrators. *Mechanical Systems and Signal*
861 *Processing* 2020;143:106812. <https://doi.org/10.1016/j.ymsp.2020.106812>.
- 862 [26] Cieplak G, Wójcik K. Conditions for self-synchronization of inertial vibrators of vibratory
863 conveyors in general motion. *Journal of Theoretical and Applied Mechanics* 2020;58:513–24.
864 <https://doi.org/10.15632/jtam-pl/119023>.
- 865 [27] Zhang X, Zhang X, Hu W, Zhang W, Chen W, Wang Z, et al. Theoretical, numerical and
866 experimental studies on multi-cycle synchronization of two pairs of reversed rotating exciters.
867 *Mechanical Systems and Signal Processing* 2022;167:108501.
868 <https://doi.org/10.1016/j.ymsp.2021.108501>.
- 869 [28] Zhang X, Zhang X, Zhang C, Wang Z, Wen B. Double and triple-frequency synchronization and
870 their stable states of the two co-rotating exciters in a vibrating mechanical system. *Mechanical*
871 *Systems and Signal Processing* 2021;154:107555. <https://doi.org/10.1016/j.ymsp.2020.107555>.
- 872 [29] Liu L, Liu T, Yue H, Zhang X. Coupling synchronization principle of two pairs counter-rotating
873 unbalanced rotors in the different resonant conditions. *Journal of Low Frequency Noise,*
874 *Vibration and Active Control* 2021;40:1149–65. <https://doi.org/10.1177/1461348420937887>.

- 875 [30] Zhang X, Wen B, Zhao C. Vibratory synchronization transmission of two exciters in a super-
876 resonant vibrating system. *J Mech Sci Technol* 2014;28:2049–58.
877 <https://doi.org/10.1007/s12206-014-0108-4>.
- 878 [31] Zhou Z. Experiment and numerical simulation of the dynamic response of subgrade bed in the
879 Wu-Guang passenger railline. Master Thesis. Central South University, 2010.
- 880 [32] Feng G, Luo Q, Wang T, Connolly DP, Liu K. Frequency spectra analysis of vertical stress in
881 ballasted track foundations: influence of train configuration and subgrade depth. *Transportation*
882 *Geotechnics* 2024;44:101167. <https://doi.org/10.1016/j.trgeo.2023.101167>.
- 883 [33] Hu J, Bian X. Analysis of dynamic stresses in ballasted railway track due to train passages at high
884 speeds. *J Zhejiang Univ Sci A* 2022;23:443–57. <https://doi.org/10.1631/jzus.A2100305>.
- 885 [34] Wang Z, Jiang G, Wei Y, Hu A. Experimental study of cyclic loading for subgrade bed of high
886 speed railway. *Rock and Soil Mechanics* 2010;31:760–4.
887 <https://doi.org/10.16285/j.rsm.2010.03.015>.
- 888 [35] Bian X, Li W, Hu J, Liu H, Duan X, Chen Y. Geodynamics of high-speed railway. *Transportation*
889 *Geotechnics* 2018;17:69–76. <https://doi.org/10.1016/j.trgeo.2018.09.007>.
- 890 [36] Zhang X. Numerical simulation and experiment study on macro-meso mechanical behaviors of
891 high-speed railway ballast. Doctor Thesis. Southwest Jiaotong Univ., 2012.
- 892 [37] Zhai W-M. Two simple fast integration methods for large-scale dynamic problems in engineering.
893 *Int J Numer Meth Engng* 1996;39:4199–214. [https://doi.org/10.1002/\(SICI\)1097-0207\(19961230\)39:24<4199::AID-NME39>3.0.CO;2-Y](https://doi.org/10.1002/(SICI)1097-0207(19961230)39:24<4199::AID-NME39>3.0.CO;2-Y).
- 895 [38] Zhai W. Vehicle–track coupled dynamics: theory and applications. Singapore: Springer Singapore;
896 2020. <https://doi.org/10.1007/978-981-32-9283-3>.
- 897 [39] Zou M, Fang P, Hou Y, Peng H, Wang D. Study on synchronization mechanism and experiment
898 of vibrating system actuated with double-frequency and dual-rotor. *Chinese Journal of*
899 *Theoretical and Applied Mechanics* 2021;53:2823–40. <https://doi.org/10.6052/0459-1879-21-359>.
- 901 [40] Li Y, Li H, Wei X, Wen B. Self-synchronization theory of a nonlinear vibration system driven by
902 two exciters. Part 1: Theoretical analysis. *Journal of Vibroengineering* 2014;16:725–34.
- 903 [41] Tang J, Liu R. *Motors and Drags*. 3rd ed. Beijing: Higher Education Press; 2014.
- 904 [42] Chen W, Ding J, Wang T, Ying Z, Wan X. An adaptive sequential sampling method based on
905 ANN_MCD and RF: Application in geotechnical problems. *Applied Soft Computing*
906 2023;110462. <https://doi.org/10.1016/j.asoc.2023.110462>.
- 907 [43] Lyu P, Luo Q, Wang T, Connolly DP. Railway gravity retaining wall design using the flower
908 pollination algorithm. *Transportation Geotechnics* 2023;42:101065.
909 <https://doi.org/10.1016/j.trgeo.2023.101065>.
- 910 [44] Yang XS. Flower pollination algorithm for global optimization. *Unconv Comput Nat Comput*
911 2012;7445:240–9.
- 912